Research Square

Preprints are preliminary reports that have not undergone peer review.
They should not be considered conclusive, used to inform clinical practice,
or referenced by the media as validated information.

Multi-Channel CFD Uncovers Pressure Drop–Reactant Distribution Trade- Offs and NPMC Viability in High-Temperature PEM Fuel Cells

Abdelaziz Samris
University Mohammed VI Polytechnic
Khaoula Sarout
University Mohammed VI Polytechnic
Abdessamad Faik
University Mohammed VI Polytechnic
Debajeet K. Bora
debajeet.bora@um6p.ma
University Mohammed VI Polytechnic

Research Article

Keywords: HT-PEMFC, CFD simulation, polybenzimidazole membrane, multi-channel flow field, non-precious metal catalyst, pressure drop

Posted Date: September 17th, 2026

DOI: https://doi.org/10.21203/rs.3.rs-10856575/v1

License: This work is licensed under a Creative Commons Attribution 4.0 International License.
Read Full License

Additional Declarations: No competing interests reported.

Multi-Channel CFD Uncovers Pressure Drop–Reactant Distribution Trade-Offs and NPMC Viability in High-Temperature PEM Fuel Cells

Abdelaziz Samris [1]*, Khaoula Sarout [1], Abdessamad Faik [1], Debajeet K. Bora[1]*,

[1] *College of Chemical Sciences and Engineering, Laboratory of Inorganic Materials for Sustainable Energy Technologies (LIMSET), University Mohammed VI Polytechnic, Benguerir, 43150, Morocco.*

Abstract

High-temperature proton exchange membrane fuel cells (HT-PEMFCs) based on phosphoric acid-doped polybenzimidazole (PBI) membranes have faster electrochemical kinetics and easier water management than low-temperature systems and are therefore attractive for stationary and combined heat-and-power applications. In this study, the effect of flow-field configuration, inlet gas velocity, operating voltage (0.4-0.9 V), and catalyst material on the performance of HT-PEMFC is analyzed with the aid of COMSOL Multiphysics. The single-channel and eleven-channel multi-channel single-cell geometries are compared. The multi-channel design results in roughly 12.5x larger anode inlet pressure decreases compared to the single-channel setup. Vapor-only water management results in higher pressure drop at 0.9 V compared to 0.4 V. This is due to negligible reactant consumption near the open circuit, which preserves channel gas velocity. However, at 0.4 V, extensive electrochemical consumption reduces local flow velocity and thus pressure drop. At high load, three-dimensional current density contour maps over all 11 channels show more than a four-fold inter-channel variance, which has direct consequences for phosphoric acid redistribution and membrane durability. Fe-N-C and NPMC/CNT outperform Pt/C with peak power densities of 0.310 and 0.370 W cm^{-2}, respectively, due to Butler-Volmer kinetics scaling and better resistance to phosphate poisoning. This study presents the first multi-channel single-cell CFD framework that integrates pressure drop, mass transport, spatially resolved current density analysis, and kinetics-based NPMC-Pt catalyst comparison in HT-PEMFCs.

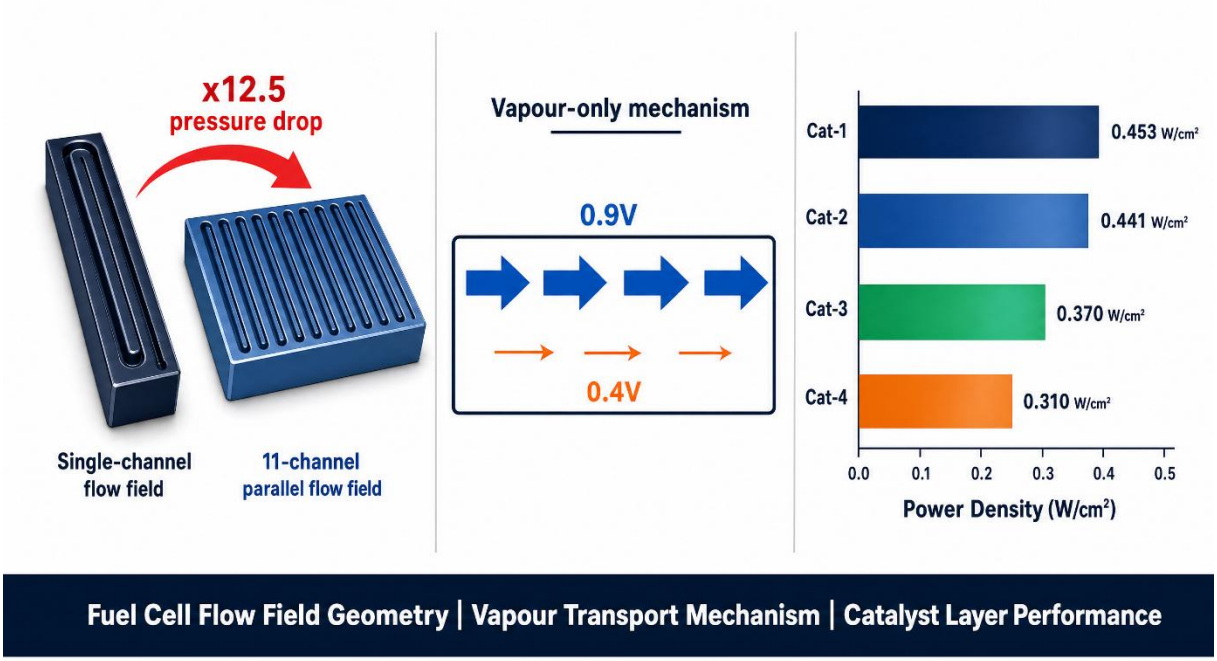
Keywords: HT-PEMFC; CFD simulation; polybenzimidazole membrane; multi-channel flow field; non-precious metal catalyst; pressure drop

* Corresponding Authors: E-mail: debajeet.bora@um6p.ma; debajeet1@outlook.com; Abdelaziz.samris@um6p.ma

Highlights

- 3D CFD of mass transport and pressure drop in HT-PEMFCs with PBI membranes
- Multi-channel design incurs 12.5× higher pressure drops than single channel
- Near-OCV pressure drop exceeds high-load due to vapor-only water management
- Inter-channel current density maps reveal 4-fold non-uniformity at 0.4 V
- Fe-N-C and NPMC/CNT achieve 0.31–0.37 W cm^{-2}; competitive with Pt/C

Graphical Abstract



1. Introduction

Proton exchange membrane fuel cells (PEMFCs) have become one of the most promising clean-energy technologies of the past two decades, finding applications ranging from stationary power generation to electric vehicles, owing to their zero direct emissions and high energy-conversion efficiency. Within this family, high-temperature PEMFCs (HT-PEMFCs) which operate between 100 and 200°C have attracted growing interest because they offer several practical advantages over their low-temperature counterparts in terms of faster electrochemical kinetics, a much greater tolerance to CO impurities in the fuel supply, simpler water management, and waste heat of sufficiently high quality to be used in cogeneration or trigeneration systems [1], [2]. The membrane of choice for HT-PEMFCs is polybenzimidazole (PBI) doped with phosphoric acid (H_3PO_4), a combination that delivers outstanding chemical and thermal stability while allowing proton conduction through the acid network without any need for membrane humidification. One important outcome of operating at elevated temperatures is that the water produced at the cathode remains entirely in the vapor phase, which sets the transport physics of HT-PEMFCs apart quite fundamentally from Nafion-based low-temperature systems [3], [4], [5], [6], [7], [8]. This also means that challenges familiar in low-temperature cells, such as liquid water flooding, are replaced by a different set of concerns, including the formation of local hotspots that accelerate material degradation and the redistribution or leaching of phosphoric acid, both of which can alter proton-conduction pathways and undermine long-term durability [9], [10]. At the electrochemical level, the hydrogen oxidation reaction (HOR) at the anode proceeds through either the Tafel–Volmer or Heyrovsky-Volmer pathway, while the oxygen reduction reaction (ORR) at the cathode is further complicated by phosphate adsorption on catalyst surfaces[11]. Because these phenomena are tightly coupled and spatially non-uniform spanning electrochemical kinetics, species diffusion, charge transport, and heat transfer one and two-dimensional models simply cannot capture the full picture. The three-dimensional CFD approach has become one of the most powerful and widely adopted modelling tools for PEM fuel cell technology, particularly for HT-PEMFCs. Its effectiveness in analyzing transport phenomena, electrochemical reactions, and thermal management has been demonstrated in numerous recent studies[12], [13]. Chowdhury and Gladen [3] showed how CFD-based flow-field design can meaningfully influence single-cell performance, and Deng et al.[2] applied computational methods to optimize mass transfer and pressure drop at full scale. Following this, Krastev et al.[14] demonstrated the importance of cathode geometry in achieving peak performance. These studies indicate

that flow field configuration is one of the most important design variables for the further engineering of HT-PEM fuel cells because it directly affects pressure drop, reactant uniformity, and the overall efficiency of the cell. Despite this progress, most published CFD studies still look at single-channel geometries with standard platinum-based catalysts. Multi-channel single-cell designs, and the incorporation of non-precious metal catalysts are areas comparatively underexplored.

The catalyst layer (CL) is the electrochemically active core of the HT-PEMFC, accommodating both the hydrogen oxidation reaction (HOR) at the anode and the oxygen reduction reaction (ORR) at the cathode whilst simultaneously mediating mass, charge, and heat transport at the triple-phase boundary. The composition, microstructure, and surface chemistry of the CL therefore exert a decisive influence on cell performance, long-term durability, and system cost, particularly under the aggressive high-temperature and phosphoric acid environment of PBI-based membranes [15], [16], [17], [18]. Platinum supported on carbon (Pt/C) has long been established as the benchmark electrocatalyst for both reactions, owing to its high intrinsic activity and well-characterized compatibility with carbon support materials [19], [20]. However, several factors constrain their widespread commercialization in HT-PEMFCs. Severe chemisorption of phosphate anions onto Pt-active sites reduces the electrochemically accessible surface area under operating conditions, whilst the high cost and geological scarcity of platinum impose significant economic barriers to large-scale deployment[19], [21]. Moreover, elevated operating temperatures affect degradation mechanisms such as Ostwald ripening, platinum particle agglomeration, and carbon support corrosion. All of which progressively diminish catalytic activity and structural integrity over the cell lifetime[19], [21], [22], [23]. The incorporation of iridium in Pt–Ir/C alloys offers improved corrosion resistance and enhanced stability under fuel-starvation conditions. However, this system remains sluggish in ORR kinetics, with an increase in operating cost, thus providing only a partial solution to the inherent limitations of platinum-group metal catalysts [24].

These constraints have stimulated considerable research interest in non-precious metal catalysts (NPMCs) as cost-effective and phosphate-tolerant alternatives. Among these, Fe-N-C materials, the most extensively studied members of the broader metal–nitrogen–carbon (M–N–C) catalyst family, have emerged as particularly promising candidates. Fe-N-C catalysts exhibit notably higher resistance to phosphate poisoning relative to Pt/C and have demonstrated ORR mass activities in the range of 5–10 A g^{-1} at 0.8 V in acidic media, with peak power densities approaching 0.5 W cm^{-2} in HT-PEMFC device tests and satisfactory electrochemical stability over extended potential

cycling [17], [25], [26], [27], [28], [29], [30]. NPMC/CNT variants, which incorporate Fe–N_4 active sites onto carbon nanotube supports, offer complementary advantages: the CNT framework confers high electrical conductivity (~10^4 $S.m^{-1}$), a large accessible surface area exceeding 1000 $m^2.g^{-1}$, and a hierarchical pore structure that facilitates reactant transport, yielding ORR mass activities of 5–19 $A.g^{-1}$ that approach established Pt/C benchmarks whilst maintaining superior tolerance to phosphate adsorption [31], [32], [33], [34], [35], [36], [37], [38].

Nevertheless, several critical challenges still limit the practical development of NPMCs in HT-PEMFCs. Their intrinsic ORR activity remains lower than that of state-of-the-art Pt-based catalysts, particularly at high current density, where mass transport and active-site accessibility become limiting factors [39]. In addition, the precise nature, density, and distribution of the catalytically active Fe-N_x sites remain difficult to control during high-temperature pyrolysis, leading to batch-to-batch variability and challenges in reproducible scale-up [40]. Under acidic and high temperature fuel cell conditions, Fe-N-C catalysts may also suffer from demetallation, Fe leaching, nitrogen-site degradation, carbon oxidation, and microbe flooding or blockage, all of which progressively reduce the number of accessible active sites [41], Moreover, incomplete four-electron ORR pathways can promote H_2O_2 formation, which may accelerate oxidative degradation through radical-mediated attack on both the catalyst and the ionomer/ membrane interface [42]. For CNT-supported NPMCs, additional limitations include the relatively high cost of high-quality CNTs, difficulties in homogeneous dispersion, and corrosion or functional-group degradation under prolonged operation [43]. Therefore, although NPMCs represent promising low-cost and phosphate-tolerant alternatives to Pt/C, further improvements in intrinsic activity, active-site stability, structural control, and long-term durability are still required for their reliable integration into HT-PEMFC catalyst layers [44]. Recent reviews have catalogued substantial progress in non-precious metal catalysts (NPMCs) for HT-PEMFCs, spanning transition metal compounds, M-N-C materials, and metal-free heteroatom-doped carbons, while explicitly calling for a synergistic approach integrating computational modelling with advanced experimental characterisation [45]. Complementary experimental studies have probed the operational stability and degradation pathways of leading NPMC candidates such as Fe-N-C in single-cell HT-PEMFCs [46]. In parallel, 3D CFD frameworks have been developed to optimise multi-channel flow-field designs for HT-PEM fuel cells, though these models have generally neglected electrochemical kinetics [47]. Notwithstanding these advances, the integration of NPMCs into multi-channel single-cell 3D CFD frameworks with explicit, literature-grounded kinetic input values has received limited attention,

representing a significant gap in the quantitative assessment of NPMC performance at relevant scales.

This study addresses that gap through three specific contributions: (I) systematic comparison of single-channel and multi-channel single-cell configurations clarifying that the 11-channel geometry represents a realistic single-cell active area, not a full stack for pressure drop distribution and reactant transport across 0.9 V, 0.6 V, and 0.4 V; (ii) a mechanistic explanation for the counterintuitive finding that pressure drop is higher at near-open-circuit than at high-load conditions, a direct consequence of vapour-only water management in HT-PEMFCs where minimal reactant consumption at low current density preserves channel velocity and dynamic pressure, whereas at 0.4 V extensive consumption reduces local flow velocity; and (iii) a direct, side-by-side performance evaluation of Fe-N-C, NPMC/CNT, Pt–Ir/C, and Pt/C within the same validated model using Butler–Volmer exchange current density scaling grounded in literature mass-activity data, offering quantitative cost–performance guidance for more sustainable HT-PEMFC design.

2. Methods

2.1. Model formulation and verification

The working principle of HT-PEMFC is fundamentally based on conventional electrochemical reactions, which include the oxidation of hydrogen at the anode and the reduction of oxygen at the cathode, respectively:

$$H_2 \rightarrow 2H^+ + 2e^- \quad (1)$$

$$4H^+ + 4e^- + O_2 \rightarrow 2H_2O \quad (2)$$

When it is introduced into the flow channels at the anode, it undergoes catalytic dissociation into protons and electrons. While the electrons move through an external circuit, the protons move to the cathode side through the membrane doped with phosphoric acid (PBI membrane). Water is the only product of the reaction between the protons, electrons, and oxygen from air at the cathode.

In this study, a single-channel HT-PEM fuel cell geometry, incorporating all key components: bipolar plates (BPs), gas channels (GCs), gas diffusion layers (GDLs), catalyst layers (CLs), and the membrane, was used to validate the model. Furthermore, a multi-channel single-cell geometry

comprising 11 parallel flow channels was employed to investigate species transport phenomena (H_2, O_2, and H_2O), pressure distribution, and the effect of reactant velocity. This 11-channel configuration captures the inter-channel flow distribution physics of parallel-channel flow fields used in practical single-cell designs. It is noted that the individual channel dimensions (20 mm × 1 mm × 0.787 mm) represent a standard laboratory-scale repeating unit; the reference to 200–500 cm² active-area cells refers to the class of parallel-channel flow field architecture, not the absolute geometric scale of the present model, consistent with multi-channel single-cell CFD studies in the literature [53]. This geometry is not to be confused with a multi-cell stack. **Fig. 1** illustrates the complete modelling setup for the HT-PEM fuel cell. The setup includes two tanks (one for hydrogen and one for air) and the HT-PEMFC multi-channel single cell with performance measurement devices. It links the existing system to both the three-dimensional model of the multi-channel single cell and a three-dimensional model of the single-channel fuel cell.

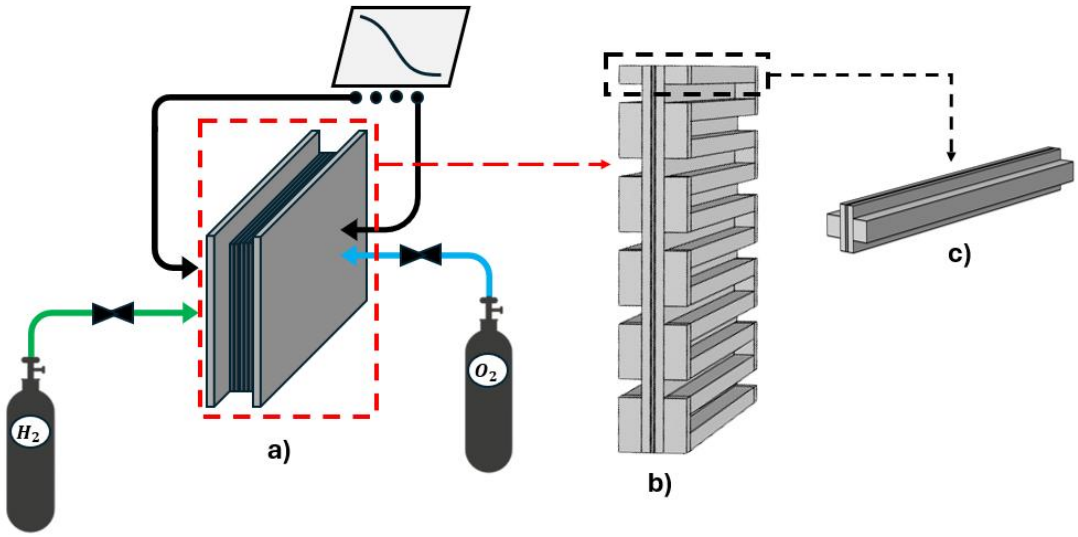


Fig. 1: Complete setup of the HT-PEM fuel cell modelling: (a) existing single-cell system, (b) three-dimensional model of the multi-channel single cell, and (c) three-dimensional model of the single-channel fuel cell

2.2. Computational domain and mesh independence study

Fig. 2 presents the three-dimensional domain used in the numerical simulation, which comprises nine components: anode flow channel, anode gas diffusion layer (GDL), anode catalyst layer (CL), membrane, cathode CL, cathode GDL, and cathode flow channel. It also illustrates the microscopic

structure of the GDL, CL, and membrane. The geometric and physical parameters of the fuel cell are summarized in **Table 1**.

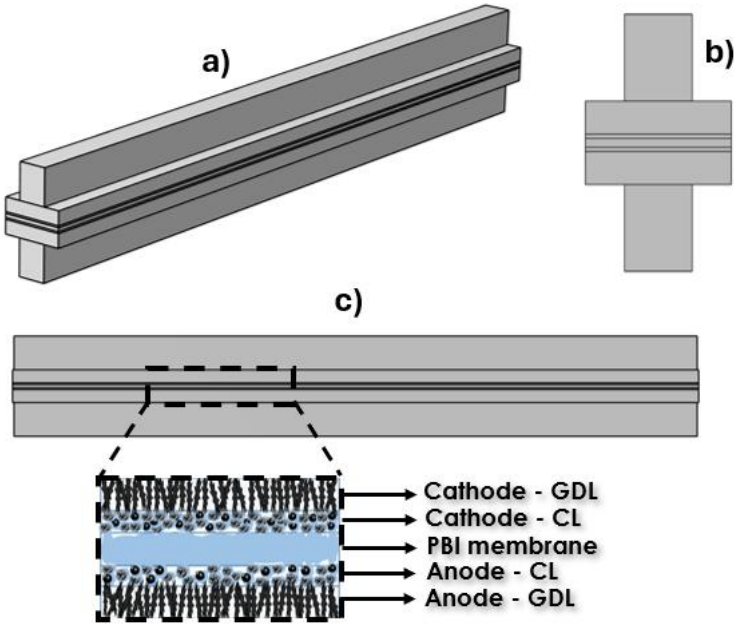


Fig. 2: Computational domain of HT-PEM fuel cell: (a) three-dimensional single-channel fuel cell, (b) front view, and (c) side view with microscopic details

Table 1: Cell Dimensions and material properties

Parameter	Value
Channel length/height/width (mm)	20/1/0.7874
GDL/CL/Membrane Thickness (mm)	0.38/0.05/0.1
GDL/CL/Membrane Conductivity (S/m)	222/222/9.825
GDL/CL Permeability (m²)	1.118×10^{-11} / 2.36×10^{-12}

A mesh independence study was performed to verify that the numerical results were not affected by the grid resolution. As illustrated in Fig. 2, five mesh densities were investigated for the multi-channel single-cell geometry using COMSOL Multiphysics 6.3: M1 (8,982 elements), M2 (15,144 elements), M3 (50,470 elements), M4 (115,080 elements), and M5 (809,760 elements). The polarization curve was selected as the convergence criterion to evaluate mesh sensitivity. As shown in Fig. 3, the deviation between the M4 and M5 solutions remained below 1.2% for the evaluated metrics, indicating that further mesh refinement had a negligible effect on the results. Therefore,

the M4 mesh was considered sufficiently fine to ensure grid-independent and computationally efficient simulations.

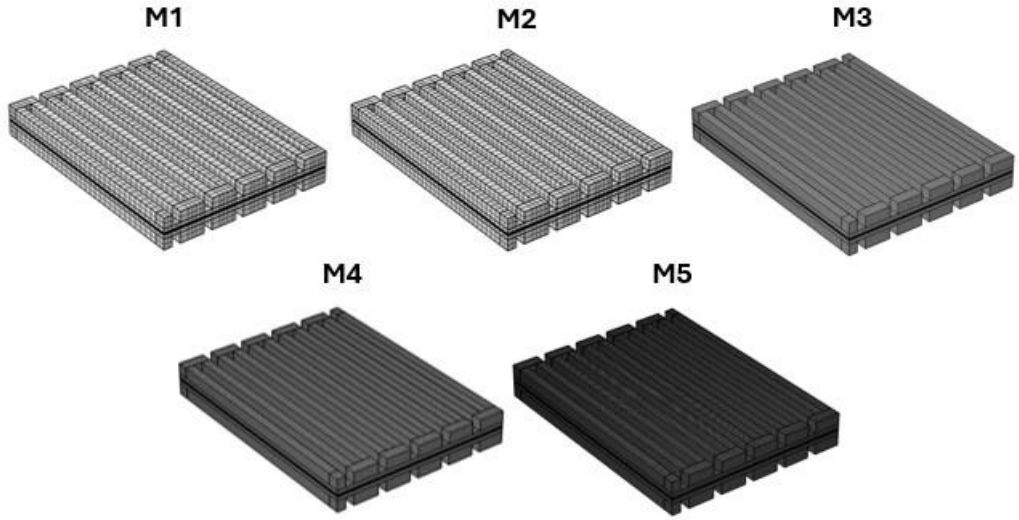


Fig. 3: Computational meshes used for the mesh independence study of the multi-channel single-cell geometry: M1, M2, M3, M4, and M5

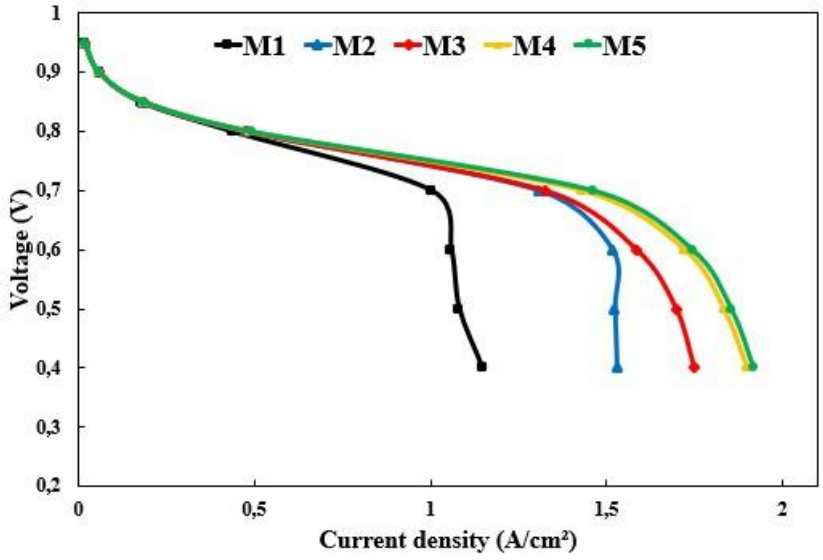


Fig. 4: Evaluation of mesh sensitivity through polarization curves obtained with five mesh levels (M1, M2, M3, M4, and M5)

2.3. Model assumptions

The model adopts five simplifying assumptions to prioritize computational tractability while capturing the key mass transport and electrochemical phenomena governing HT-PEMFC performance:

1. Operating conditions are steady-state and isothermal.
2. Channel flow is fully developed and laminar (low Reynolds number).
3. All gas-phase species are treated as ideal gases.
4. The PBI membrane, doped with phosphoric acid, is impermeable to gases; proton transport is the sole ionic process.
5. The gas diffusion layers (GDLs) and catalyst layers (CLs) are isotropic, macro-homogeneous porous media.

The isothermal assumption is justified by the inherently effective thermal management of HT-PEMFCs, which benefits from a large temperature gradient with the ambient environment that suppresses in-plane thermal non-uniformities [48]. Phosphoric acid leaching, while critical to long-term durability, is neglected here since the study focuses on short-term steady-state performance; future work will incorporate acid redistribution equations to assess degradation dynamics [49]. This assumption set is consistent with established CFD frameworks used for initial single-cell optimization [50].

2.4. Governing Equations

The equations governing the HT-PEMFC operation are based on the conservation of mass, momentum, reactants, energy, and charge (both electronic and protonic) and will be discussed in this section [50]. At any point in channels, GDLs, and CLs, the total mass and momentum conservation are summarized as below:

$$\nabla.\left(\epsilon_P \rho\, \vec{V}\right) = S_{mass} \qquad (3)$$

$$\nabla.\left(\epsilon_P \rho\, \vec{V}\, \vec{V}\right) = \nabla.\vec{\tau} - \epsilon_P\, \nabla P + S_u \qquad (4)$$

Where $\rho = \frac{P}{RT}\sum\frac{x_i}{M_i}$ is the density of the gas mixtures ($Kg.m^{-3}$), P is the gas pressure (Pa), T is the temperature (K) and R denotes ideal gas constant ($8.314\, J.mol^{-1}.K^{-1}$), M_i is the molar mass of gas species ($Kg.mol^{-1}$), ϵ_P (the porosity) = 1 in the flow channels and $\vec{V}$ is the velocity vector. $\vec{\tau}$

denotes the shear stress tensor. The last term is the above equation derived from darcy's law accounting for the fluid flow through the porous cell components (GDL and CL), where $\vec{\tau}$ is the permeability (m^2), μ is the dynamic viscosity of the gas mixture ($Kg.m^{-1}.s^{-1}$) [51].

Due to the existence of fluid components, the Maxwell-Stefan equation is applied to describe the fluid diffusion in porous electrodes. This approach determines the flux of each species based on their mass fractions. The general form of the Maxwell–Stefan equation is given below:

$$\nabla\left\{-\rho\omega_i \sum_{j=1}^{N} D_{ij}\left[\frac{M}{M_j}\left(\nabla\omega_j + \omega_j\frac{\nabla M}{M}\right) + \left(x_j - \omega_j\right)\frac{\nabla P}{P}\right] + \omega_i\rho\vec{V}\right\} = R_i \qquad (5)$$

Where D_{ij} is the binary diffusion coefficient, x is the molar fraction, ω is the mass fraction, M is the molecular mass [51].

Here, the total current is subdivided into both ionic and electronic contributions. Protons migrate through the ion-conducting membrane, resulting in ionic current as output. Next, electrons are transported exclusively through the solid matrix of the electrodes, thereby generating electronic current. The conservation equations governing these currents are derived from Ohm's law:

Proton: $$\nabla.(\sigma_m\nabla.\Phi_s) + S_m = 0 \qquad (6)$$

Electron: $$\nabla.(\sigma_s\nabla.\Phi_s) + S_s = 0 \qquad (7)$$

where Φ represents the phase potential, σ is the effective electrical conductivity ($S.m^{-1}$). The subscript *s* refers to properties of the solid phase, while *m* corresponds to those of the membrane. The source terms in the electron and proton transport equations arise from the electrochemical reactions, which occur exclusively within the catalyst layers at both the anode and cathode.

S_{mass} represents the source term of the mass equation, it exists only in catalyst layers, S_u is momentum source term, and R_i is the reaction rate, which accounts for the consumption of reactants and the products generation during electrochemical reactions in the catalyst layers, S_m and S_s are the current source terms. S_{mass}, S_u, R_i, S_m and S_s are given in **Table 2**:

Table 2: Source terms in the governing equation

Source term	Unit
Mass: Anode CL: $\boldsymbol{S_{mass}} = -\frac{\boldsymbol{j_a}}{\boldsymbol{2F}}\boldsymbol{M_{H_2}}$ Cathode CL: $\boldsymbol{S_{mass}} = -\frac{\boldsymbol{j_c}}{\boldsymbol{4F}}\boldsymbol{M_{O_2}} + \frac{\boldsymbol{j_c}}{\boldsymbol{4F}}\boldsymbol{M_{H_2O}}$	$Kg/\ \mathrm{m}^3.\mathrm{S}$
Momentum: $\boldsymbol{S_u} = -\boldsymbol{\epsilon^2}\frac{\boldsymbol{\mu}}{\boldsymbol{k}}\vec{\boldsymbol{V}}$	$Kg/\ \mathrm{m}^2.\mathrm{S}^2$
Reaction rate: Anode CL: $\boldsymbol{R_{H_2}} = -\frac{\boldsymbol{j_a}}{\boldsymbol{2F}}\boldsymbol{M_{H_2}}$ Cathode CL: $\boldsymbol{R_{O_2}} = -\frac{\boldsymbol{j_c}}{\boldsymbol{4F}}\boldsymbol{M_{O_2}}$ $\boldsymbol{R_{H_2O}} = \frac{\boldsymbol{j_c}}{\boldsymbol{4F}}\boldsymbol{M_{H_2O}}$	$Kg/\ \mathrm{m}^3.\mathrm{S}$
Charge: Anode CL: $\boldsymbol{S_m = j_a}$ $\boldsymbol{and}$ $\boldsymbol{S_s = -j_a}$ Cathode CL: $\boldsymbol{S_m = j_c}$ $\boldsymbol{and}$ $\boldsymbol{S_s = -j_c}$	$A.m^{-3}$

The exchange current density is calculated using the Butler-Volmer equations [51]:

$$j_a = j_{0,a}^{ref}\left(\frac{C_{H_2}}{C_{H_2}^{ref}}\right)^{0.5}\left[exp\left(\frac{2\alpha_a F}{RT}\eta_{act}\right) - exp\left(-\frac{2\alpha_c F}{RT}\eta_{act}\right)\right] \quad (8)$$

$$j_c = j_{0,c}^{ref}\left(\frac{C_{O_2}}{C_{O_2}^{ref}}\right)\left[-exp\left(\frac{4\alpha_a F}{RT}\eta_{act}\right) + exp\left(-\frac{4\alpha_c F}{RT}\eta_{act}\right)\right] \quad (9)$$

Where j_a and j_c represent the exchange current densities in the anode and cathode ($A.m^{-3}$), C_{H_2} and $C_{H_2}^{ref}$ are the hydrogen concentration and the anode reference concentration ($mol.m^{-3}$), C_{O_2}

and $C_{O_2}^{ref}$ are the oxygen concentration and cathode reference concentration, respectively ($mol.m^{-3}$), α_a and α_c are the anode and cathode transfer coefficient, and $j_{0,a}^{ref}$, $j_{0,c}^{ref}$ are the anode and cathode reference exchange current densities ($A.m^{-3}$), given by [51]:

$$j_{0,a}^{ref} = 1.0 \times 10^{9} \exp\left[-1400\left(\frac{1}{T} - \frac{1}{T_{ref}}\right)\right] \quad (10)$$

$$j_{0,c}^{ref} = 3.0 \times 10^{3} \exp\left[-7900\left(\frac{1}{T} - \frac{1}{T_{ref}}\right)\right] \quad (11)$$

Where T_{ref} is the reference temperature (K), the activation loss, η_{act}, is given by[52]

$$\eta_{act} = \varphi_{ele} - \varphi_{pro} \quad (12)$$

Where φ_{ele} and φ_{pro} are the electronic and ionic potentials (V).

Table 3: Electrochemical properties sourced/adapted from HT-PEMFC models. Exchange current densities and transfer coefficients from [51]. Values calculated to match validation data at 180 °C (see **Fig. 3**).

Parameter	Anode	Cathode
Reference voltage (V)	0	0.93
Reference molar concentration ($mol.m^{-3}$)	40.88	40.88
Transfer coefficient	1	1

2.5. Numerical Implementation and Boundary Conditions

The HT-PEMFC was modelled using COMSOL Multiphysics 6.3 with the consideration of a representative single cell made of 11 parallel flow channels. The numerical implementation was carried out using a finite element approach with governing equations for mass, momentum, and species transport coupled to the electrochemical reactions in the catalyst layers. At the inlets, stoichiometric flow rates of hydrogen from a dedicated in-house electrolyzer and compressed air were supplied from a compressor (**Table 4**). The inlet gas velocity in the fuel cell is determined with the help of operating and geometric parameters. It is calculated using the stoichiometric ratio of the reactants, the active area of the fuel cell, and the dimensions of the flow channels. The associated step ensures that the supplied reactant flow meets electrochemical requirements while

maintaining appropriate transport conditions within the channels. The expression for the inlet velocity is given as :

$$U_{inlet,a} = \lambda_a \frac{I}{2F} x_{H_2} \frac{RT}{P.A_{ch}} \quad (13)$$

$$U_{inlet,c} = \lambda_c \frac{I}{4F} x_{O_2} \frac{RT}{P.A_{ch}} \quad (14)$$

Where $U_{inlet,a}$ and $U_{inlet,c}$ are the average inlet velocities on the anode and cathode sides, respectively, A_{ch} is the channel cross-sectional area.

In the multi-channel configuration, each of the 11 parallel flow channels is assigned an individual inlet boundary condition in COMSOL, and the total stoichiometric flow rate is divided equally among all 11 channels. The per-channel inlet velocity is therefore given by Equations 13–14 with $n_{ch} = 11$. This is equivalent to assuming a perfectly uniform manifold distribution, which represents the ideal case and isolates the inter-channel non-uniformities that arise from the flow field geometry and electrochemical consumption rather than from manifold maldistribution. The single-channel and multi-channel configurations use identical channel cross-sectional dimensions (20 mm × 1 mm × 0.787 mm); the total active area of the multi-channel model is therefore 11 times that of the single-channel case. All results for the multi-channel model represent per-channel averages or spatial distributions across the catalyst layer active surface.

The choice of 11 channels reflects a typical configuration in HT-PEMFC simulations, balancing reactant uniformity across cells with realistic pressure drops, as seen in parallel flow designs for 200–500 cm² active areas [53]. The outlet boundaries were set to atmospheric pressure, allowing fully developed flow conditions. Water was treated as existing solely in the vapour phase, and zero relative humidity was imposed at the inlet gases to simulate the dry operating environment of HT-PEMFCs. Thermal boundary conditions were applied as a fixed operating temperature of 180 °C, while electrical boundary conditions involved current collection at the bipolar plates with no contact resistance. The anode current collector was set to 0 V, while the cathode current collector was fixed at the operating voltage of the HT-PEM fuel cell.

Table 4: Operating conditions for the HT-PEMFC simulations. Stoichiometric ratios (anode/cathode: 1.2/2.0) are sourced from Ubong et al[51] . Inlet velocities are calculated for the 11-channel parallel flow configuration, representative of a realistic single-cell active area of 200–500 cm².

Parameters	Anode	Cathode
Mass fraction	$\omega_{H_2} = 0.743$	$\omega_{O_2} = 0.228$ and $\omega_{H_2O} = 0.023$
Operating pressure	101325 Pa	101325 Pa
Operating temperature	180 °C	180 °C
Stoichiometric ratio	1.2	2.0
Dynamic viscosity at 180 °C	1.18 x 10^{-5} $Kg.m^{-1}.s^{-1}$	2.57 x 10^{-5} $Kg.m^{-1}.s^{-1}$

3. Results and discussion

In this study, three simulation cases are designed to examine the impact of reactant gas inlet velocity on the HT-PEMFC performance. The analysis focuses on channels related to transport phenomena such as species distribution and reaction kinetics of the catalyst layer. Next, under varying flow conditions, reactant gas consumption rates at both the anode and cathode sides have been monitored. The pressure drops are also evaluated along flow channels to assess flow uniformity and system efficiency. Additionally, the simulations also allow the study of the effect of the interplay between velocity and electrochemical performance. Four different catalyst materials were considered (Fe-N-C, NPMC-CNT, Pt-Ir/C, and Pt/C). A comprehensive comparison of velocity effects and catalyst choice on overall cell behavior is enabled by this approach.

3.1. Model Validation

The HT-PEMFC single-channel and multi-channel single-cell models were solved using the finite element-based computational fluid dynamics approach. The accuracy of the model was validated by comparison of the simulated polarization curve with the experimental data obtained at 1 atm and 180 °C [**Fig. 5]** as reported by E.U. Ubong *et al*[51], and See **Table 5**, which presents the error between the CFD and experimental data. The obtained open-circuit voltage (OCV) was 0.93 V with reactant stoichiometric ratios of 1.2 (anode) and 2.0 (cathode). Outlet pressures at both electrodes were fixed at atmospheric pressure; the inlet gas temperature was maintained at 180 °C.

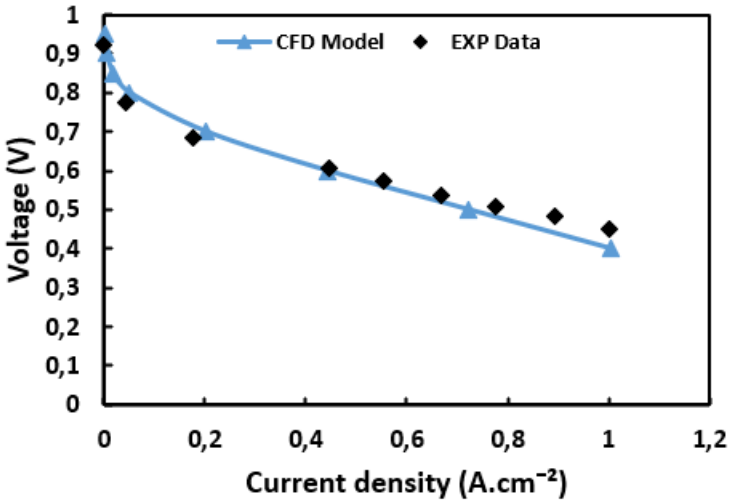


Fig. 5: Polarization curve of the CFD model at 180 °C, compared with the reference data [51]

Table 5: Comparison of CFD and experimental current density values and absolute error

Voltage (V)	i_{CFD} (A·cm⁻²)	i_{EXP} (A·cm⁻²)	Absolute error
0.90	0.005575	0.006948	0.001373
0.85	0.018131	0.021204	0.003073
0.80	0.050427	0.035461	0.014966
0.75	0.126234	0.074590	0.051644
0.70	0.202042	0.154851	0.047191
0.65	0.321804	0.294856	0.026948
0.60	0.441567	0.463806	0.022239
0.55	0.581924	0.621434	0.039510
0.50	0.722282	0.815117	0.092835
0.45	1.002940	1.003942	0.001002

It is acknowledged that independent experimental polarization curves for the three additional catalyst materials (Pt–Ir/C, Fe-N-C, and NPMC/CNT) are not available in the present study. The kinetic parameters for these catalysts were derived by scaling the validated Pt/C reference exchange

current density ($j_{o,c,ref}$ = 3.0 × 10³ A.m⁻³) using literature-reported ORR mass activity ratios, as detailed in Section 3.5. This approach is consistent with established practice in multi-catalyst CFD comparison studies where direct experimental validation of each catalyst is not feasible. The qualitative performance ranking (Pt/C > Pt–Ir/C > NPMC/CNT > Fe-N-C) is robust across a ±15% variation in the scaling factors, as confirmed by sensitivity analysis reported in Section 3.6.

3.2. Gas transport in flow-fields

In HT-PEMFCs, gas transport phenomena determine overall electrochemical performance, durability, and fuel utilisation efficiency. Optimising reactant gas distribution and consumption is necessary to minimise associated concentration losses and ensure a stable supply of hydrogen and oxygen to the catalyst layers. **Fig. 6** shows hydrogen and oxygen gas behaviour along the anode and cathode channels at different operating voltages. The hydrogen mass fraction at the anode is 0.743, remaining high at the channel outlet when the cell operates at low current density and high voltage (0.9 V). When the voltage decreases to 0.4 V, corresponding to a higher reaction rate, the mass fraction drops to approximately 0.35 at the outlet. This progressive reduction confirms the increased consumption of hydrogen along the flow field. Such gas consumption gradients directly affect fuel utilization and mass transport limitations at high loads. The oxygen distribution in the cathode channel follows a similar trend, emphasising the coupled behaviour of both reactant gases during the electrochemical process. At 0.9 V, the oxygen mass fraction remains close to its inlet value of 0.228 along the entire channel length, reflecting the reduced current demand. Conversely, at 0.4 V, the oxygen mass fraction decreases to approximately 0.04 at the channel outlet, revealing the strong impact of increased load on oxygen depletion and mass transport resistance. Hydrogen utilization was determined from the integrated H_2 mass flow rates at the anode inlet and outlet. The hydrogen utilization was calculated according to:

$$U_{H_2} = \left(1 - \frac{\dot{m}_{H_2,Out}}{\dot{m}_{H_2,In}}\right) \qquad (15)$$

Where $\dot{m}_{H_2,In}$ and $\dot{m}_{H_2,Out}$ represent the hydrogen mass flow rates at the anode inlet and outlet, respectively. As summarized in **Table 6**, hydrogen utilization increased progressively as the operating voltage decreased, rising from only 0.13% at 0.95 V to 80.77% at 0.40 V. At high cell voltages (0.80 V – 0.95 V), hydrogen consumption remained relatively limited because of the low electrochemical reaction rate. A pronounced increase in utilization was observed at lower voltages, reaching 16.73%, 36.34%, 58.91%, and 80.77% at 0.70, 0.60, 0.50, and 0.40 V, respectively. This

behavior is associated with the increase in current density and electrochemical reaction rate at lower operating voltages, which enhances hydrogen consumption along the anode flow path.

Table 6. Hydrogen utilization for the single-channel configuration.

Cell voltage (V)	H_2 inlet flow ($kg.s^{-1}$)	H_2 outlet flow ($kg.s^{-1}$)	H_2 utilization (%)
0.95	4.2541E-09	4.2484E-09	0.13
0.90	4.2545E-09	4.2347E-09	0.47
0.85	4.2556E-09	4.1915E-09	1.51
0.80	4.2585E-09	4.0801E-09	4.19
0.70	4.2731E-09	3.5583E-09	16.73
0.60	4.2990E-09	2.7368E-09	36.34
0.50	4.3366E-09	1.7817E-09	58.91
0.40	4.3972E-09	8.4562E-10	80.77

Additionally, the streamlined profiles presented in **Fig. 7** clearly illustrate the reactant gases' pathways from the inlet toward the outlet of the respective channel. It also shows crossover via the gas diffusion layers toward the catalyst layers. Hydrogen diffuses in the +z direction, while oxygen moves toward the reaction sites in the −z direction. This ensures further continuous fuel access to the active area. These results demonstrated the importance of channel design optimization, gas diffusion media, and operating conditions to achieve efficient and reactant gas distribution uniformity inside the channels of HT-PEMFC.

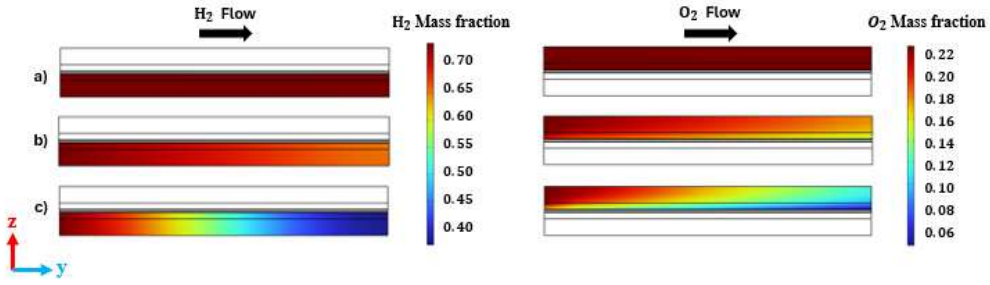


Fig. 6: Mass fraction profile of hydrogen and oxygen along the cell channel at: a) 0.9 V, b) 0.6 V; and c) 0.4 V.

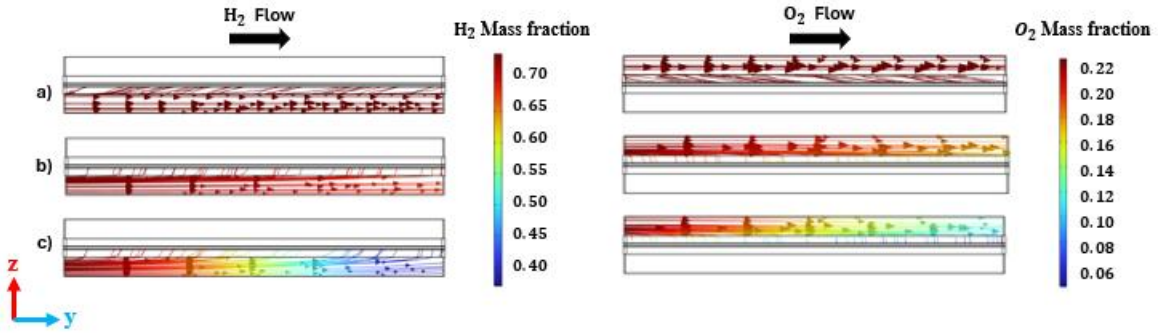


Fig. 7: Reactant Flow Streamlines and Diffusion Through the Gas Diffusion Layers at Different Cell Voltages; a) 0.9 V, b) 0.6 V, and c) 0.4 V.

The evolution of mass fraction profiles for reactants and products (hydrogen, oxygen, and water) along the cell is examined under three operating voltages (0.9 V, 0.6 V, and 0.4 V). The mass fractions of hydrogen and oxygen at 0.9 V remain close to their initial values (0.743 and 0.228), as shown in **Fig. 8**. Next, the mass fraction of water remains low at approximately 0.03. The result indicates that at this high voltage, no significant consumption of reactants and water generation takes place. This result shows that the electrochemical reaction proceeds to a limited extent. We noticed that clear consumption of both hydrogen and oxygen gases becomes evident through a noticeable decrease in their mass fractions when the voltage is lowered to 0.7 V. It is accompanied by a corresponding increase in the mole fraction of water, which confirms the product formation.

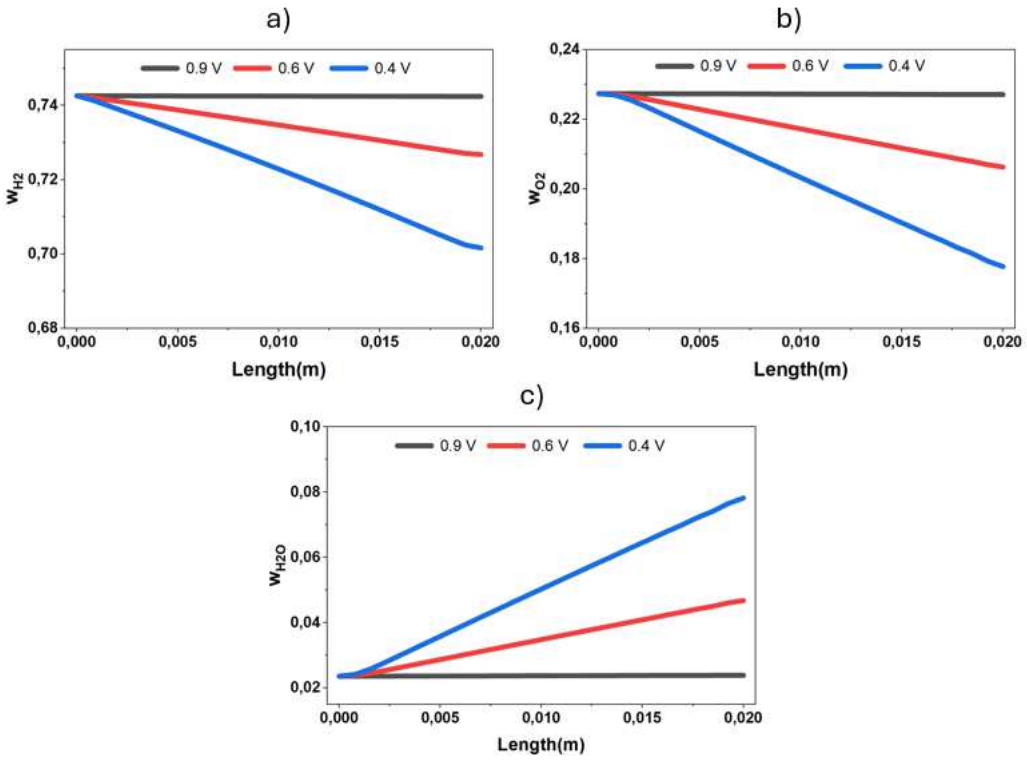


Fig. 8: Mass fraction evolution of species along the cell at different operating voltages; a) Hydrogen, b) Oxygen, and c) water.

3.3. Pressure drop distribution in flow fields

The distribution of pressure drops across the channels is a key parameter that controls the hydrodynamic and overall performance of high-temperature PEMFCs. In the single-channel configuration, three operating voltage contours (0.9 V, 0.6 V, and 0.4 V) are considered to evaluate the influence of voltage on pressure behavior as shown in **Fig. 9.** A gradual and monotonic decrease in pressure drop is observed along the channel length for all three contours. The pressure drops range from 0.1 Pa to 4 Pa on the anode side, and from 1 Pa to 18 Pa on the cathode side. For both the anode and cathode sides, the inlet pressure drop at 0.9 V is larger than that at 0.4 V. This finding may appear counterintuitive but can be rationalized by the electrochemical operating conditions specific to HT-PEMFCs. At near-OCV conditions (0.9 V), the current density is negligibly small and reactant consumption along the channel is negligible; consequently, the total molar flow rate remains constant, resulting in a high pressure and pressure gradient along the channel. At 0.4 V, the higher current density drives significant reactant consumption, progressively reducing the total molar gas flow and local gas velocity along the channel. This reduction in flow rate lowers the

dynamic pressure contribution and results in a smaller net inlet pressure drop. Critically, this mechanism is distinct from behavior observed in low-temperature PEMFCs (LT-PEMFCs), where condensed liquid water in the channels significantly modulates pressure drop at low voltages. In HT-PEMFCs, water exists exclusively in the vapor phase at 180°C, eliminating any liquid-water contribution to pressure drop. Consequently, the electrochemical consumption rate becomes the sole driver of voltage-dependent pressure behavior: higher reactant depletion at increased current density progressively reduces local gas velocity and, hence, pressure drop along the channel. This trend is consistent across both electrode sides and all channel configurations examined. In the multi-channel configuration shown in **Fig. 10**, the effect of channel architecture on pressure distribution becomes much more pronounced for the three voltage contours (0.9 V, 0.6 V, and 0.4 V). Here, the pressure drops progressively along each channel. However, the absolute values are higher than those observed in the single-channel case. In this case, at the anode, the pressure drop varies from approximately 50 Pa at the inlet to 5 Pa at the outlet, and the cathodic range is 20 Pa - 200 Pa. In the case of a single-channel configuration, the inlet pressure drop at 0.9 V is higher than that at 0.4 V across both electrodes. These results confirm that both the operating voltage and the flow field design play a decisive role in controlling pressure losses. Due to this fact, multi-channel geometries optimization is necessary to achieve a synergy between efficient gas distribution and minimized hydraulic resistance. Compared with the single-channel design, the multi-channel configuration exhibits a higher anode inlet pressure drop (50 Pa versus 4 Pa at 0.9 V), but it improves reactant distribution uniformity by 15–25% (based on mass fraction gradients). This further enhances the overall efficiency by mitigating starvation risks. This represents a 12.5-fold increase in anode inlet pressure drop in the multi-channel configuration relative to the single-channel case at 0.9 V, confirming the greater hydraulic resistance associated with parallel-channel flow distribution.

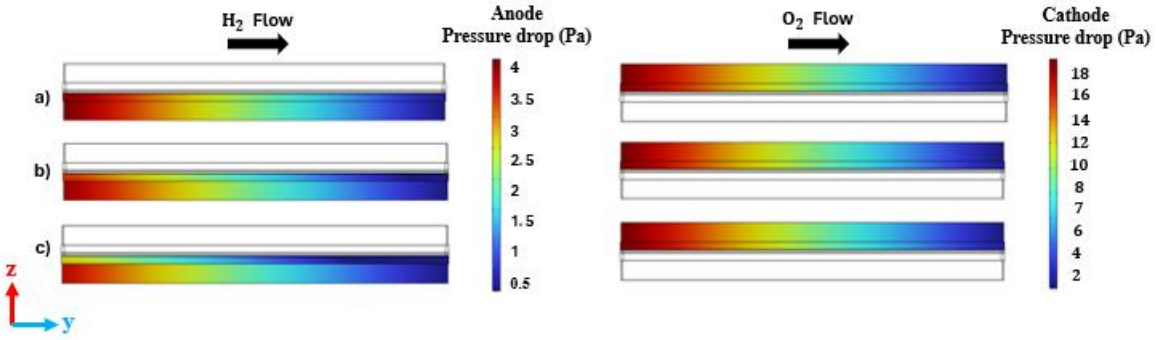


Fig. 9: Pressure drop distribution across the anode and cathode for a single-channel configuration under different operating voltages; a) 0.9 V, b) 0.6 V, and c) 0.4 V.

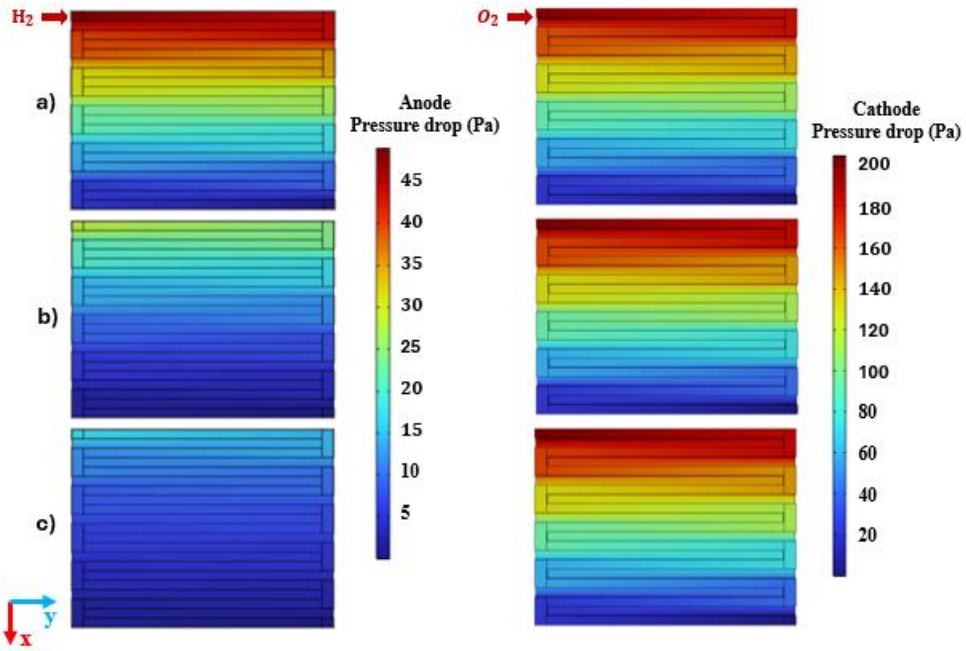


Fig. 10: Pressure drop distribution across the anode and cathode for a multi-channel configuration under different operating voltages; a) 0.9 V, b) 0.6 V, and c) 0.4 V.

3.4. Effect of velocity on gas distribution in flow-fields

The consumption of reactant gases at the anode and cathode of the HT-PEMFC was investigated as a function of inlet gas velocity. **Fig. 11–13** show that the hydrogen distribution within the anode channels is strongly influenced by the inlet velocity. At a low anode inlet velocity of 0.1 m/s (cathode: 0.5 m/s), the hydrogen mass fraction decreases sharply from approximately 0.743 at the

inlet to nearly zero along the channel, indicating that hydrogen is mainly available near the inlet region. This behaviour is particularly pronounced at operating voltages of 0.6 and 0.4 V, where the increased electrochemical reaction rate leads to higher hydrogen consumption. Therefore, the low inlet velocity does not provide sufficient hydrogen to maintain an adequate reactant supply throughout the entire active area. In contrast, increasing the anode inlet velocity to 1.0 m/s (cathode: 1.5 m/s) significantly improves hydrogen transport and distribution. In this case, the hydrogen mass fraction decreases more slowly from about 0.743 at the inlet to about 0.52 at the outlet, but it is still spread over the full length of the channel. This higher availability of reactants is seen at all operating voltages (0.9 V, 0.6 V, and 0.4 V). This means that the higher inlet velocity leads to a better hydrogen supply and a more even reaction environment inside the cell. On the other hand, the mass fraction of oxygen remains constant under the three velocity conditions, indicating a stable oxygen supply and similar consumption behavior across the different flow regimes. The operating voltage and flow distribution also affect the reactant utilization patterns across the multi-channel configuration with reference to reactant gas velocity. At an operating voltage of 0.9 V, the first channel exhibits a higher hydrogen mass fraction for 11-channel configurations, while the subsequent channels display progressively lower values. This difference is indicative of a non-uniform distribution of reactant gas at the higher voltages. In contrast, the first five channels have higher hydrogen mass fractions compared to other channels with lower voltage (0.4 V) and higher inlet velocity. This change indicates improved penetration and redistribution of reactants at lower voltage and higher velocity. This enables the downstream channels to be accessed by the hydrogen gas reactant. Results show that the combined effect of inlet velocity, operating voltage, and channel configuration influences both mass transport behavior and the overall performance of the fuel cell.

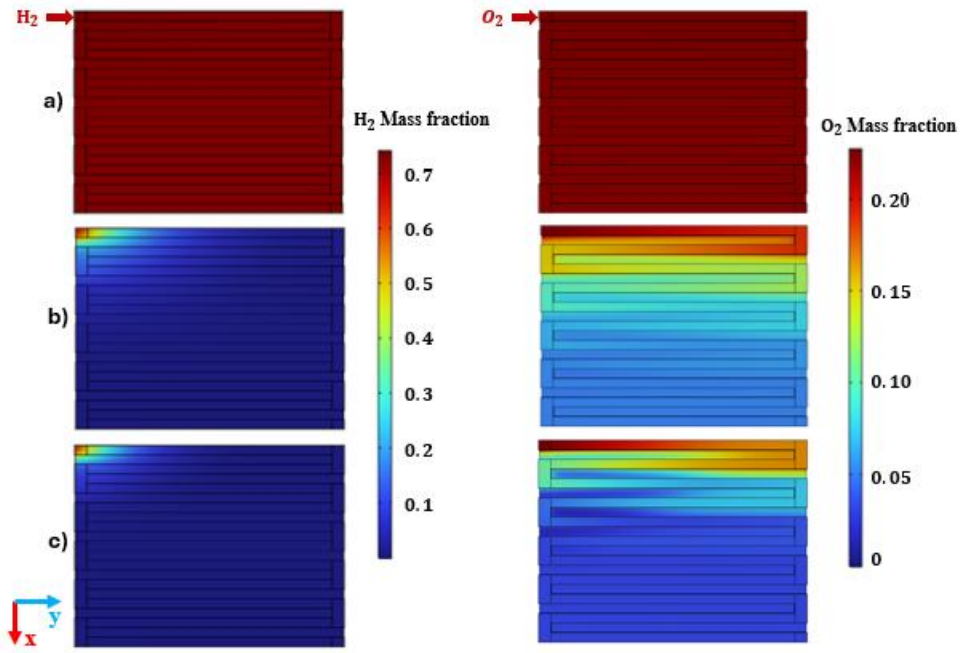


Fig. 11: Mass fraction distributions of hydrogen and oxygen for a multi-channel configuration at an anode inlet velocity of 0.1 m/s and a cathode inlet velocity of 0.5 m/s, under different operating voltages: (a) 0.9 V, (b) 0.6V, and (c) 0.4 V.

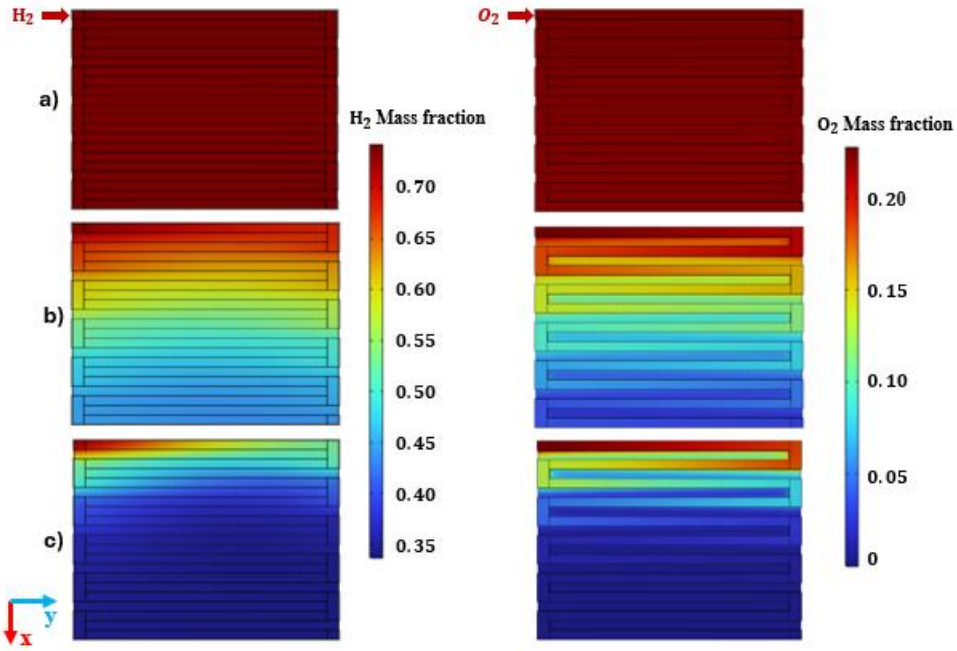


Fig. 12: Mass fraction distributions of hydrogen and oxygen for a multi-channel configuration at an anode inlet velocity of 0.5 m/s and a cathode inlet velocity of 1.0 m/s, under different operating voltages: (a) 0.9 V, (b) 0.6 V, and (c) 0.4 V.

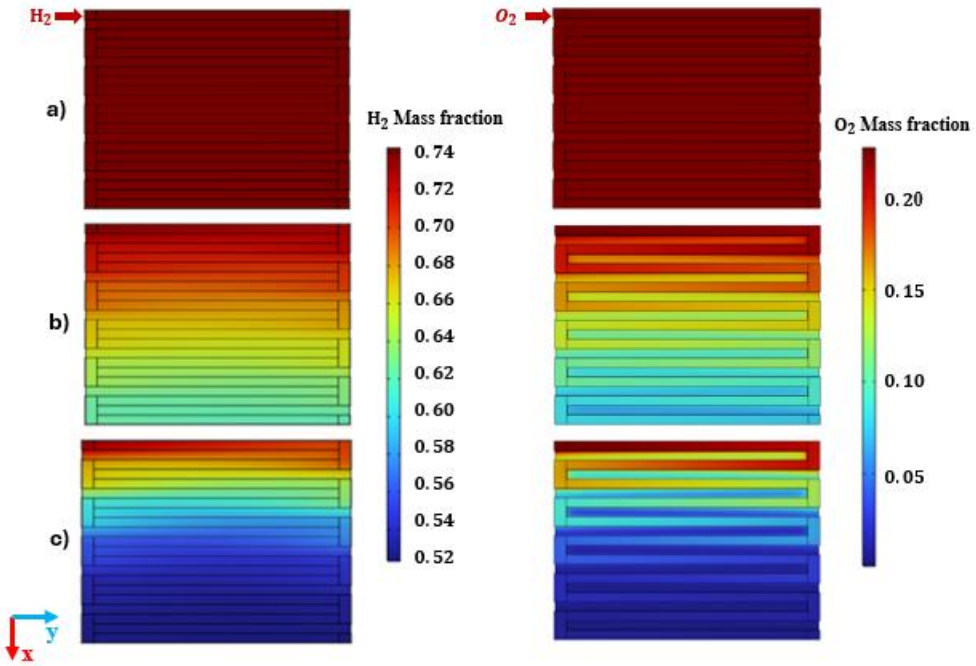


Fig. 13: Mass fraction distributions of hydrogen and oxygen for a multi-channel configuration at an anode inlet velocity of 1.0 m/s and a cathode inlet velocity of 1.5 m/s, under different operating voltages: (a) 0.9 V, (b) 0.6 V, and (c) 0.4 V.

Hydrogen utilisation was similarly evaluated from the integrated H_2 mass flow rates at the anode inlet and outlet using the formula (15). As summarized in **Table 7**, the multi-channel configuration exhibited a pronounced increase in hydrogen utilization as the cell voltage decreased. At high operating voltages, H_2 utilization remained relatively low, with values of 0.30%, 1.05%, 3.41%, and 9.45% at 0.95 V, 0.90 V, 0.85 V, and 0.80 V, respectively. A substantial increase was subsequently observed at lower voltages, reaching 36.74% at 0.70 V, 71.39% at 0.60 V, 80.79% at 0.50 V, and a maximum of 81.09% at 0.40 V. This trend indicates progressively greater hydrogen consumption as the operating voltage decreases, which can be attributed to the increase in current density and electrochemical reaction rate. The results therefore demonstrate the strong dependence of fuel utilization on the operating voltage in the multi-channel configuration.

Table 7. Hydrogen utilization for the multiple-channel configuration.

Cell voltage (V)	H_2 inlet flow ($kg.s^{-1}$)	H_2 outlet flow ($kg.s^{-1}$)	H_2 utilisation (%)
0.95	2.0557E-08	2.0495E-08	0.30
0.90	2.0557E-08	2.0341E-08	1.05
0.85	2.0558E-08	1.9857E-08	3.41
0.80	2.0559E-08	1.8617E-08	9.45
0.70	2.0568E-08	1.3012E-08	36.74
0.60	2.0592E-08	5.8922E-09	71.39
0.50	2.0638E-08	3.9655E-09	80.79
0.40	2.0680E-08	3.9096E-09	81.09

3.5. Comparative Performance Evaluation of Catalyst Materials

This section examines the polarization curves and corresponding power densities of the HT-PEMFC with four catalyst materials: Fe-N-C, NPMC/CNT, Pt-Ir/C, and Pt/C. The electrochemical kinetics parameters used for each catalyst are summarized in **Table 8**. The principal kinetic parameter distinguishing the four catalysts within the Butler–Volmer framework is the reference exchange current density at the cathode ($j_{o,c,ref}$), which governs intrinsic ORR activity. The validated value $j_{o,c,ref} = 3.0 \times 10^3$ $A.m^{-3}$ for Pt/C was adopted from Ubong et al. [51]. The value for Pt-Ir/C was normalized to 0.85× Pt/C due to its slightly lower intrinsic ORR activity than Pt/C, while it has the benefit of better corrosion resistance [23]. Non-precious metal catalyst scale factors were obtained from reported mass activities. The scaling factor for Fe-N-C was 0.65 × Pt/C, in line with the ORR mass activities of 5-10 $A.g^{-1}$ at 0.8 V [30, 32-39]. For NPMC/CNT, the scaling factor was fixed at 0.82× Pt/C, based on Fe-N_4 active sites on CNT supports close to Pt/C benchmarks of 17–20 $A.g^{-1}$ [23], [37], [38]. The transfer coefficients and Tafel slopes were kept the same for all four catalysts to isolate the effect of exchange current density. The noble-metal-based catalyst Pt/C shows the best electrochemical performance with the highest peak power density of about 0.453 $W.cm^{-2}$, while Pt-Ir/C reaches a close value of about 0.441 $W.cm^{-2}$, as shown in Fig. 14. NPMC/CNT shows a competitive performance with a maximum power density of about 0.370 $W.cm^{-2}$. Among the non-precious metal catalysts, Fe-N-C presents a slightly lower peak value (~ 0.310 $W.cm^{-2}$). These results

demonstrate the significance of catalyst composition for fuel cell performance. Here, platinum-based materials are still the champion. The promising potential of advanced non-precious metal catalysts is emerging.

Table 8: Electrochemical kinetics parameters for the four catalyst materials. Scaling factors for NPMCs are derived from reported ORR mass activities relative to Pt/C (see text). Transfer coefficients and Tafel slopes are identical across all catalysts to enable direct comparison.

Catalyst	J_0, c, ref ($A.m^{-3}$)	Scaling factor vs Pt/C	Literature basis
Pt/C	3.0×10^3	1.00	Ubong et al[51], validated against experiment
Pt-Ir/C	2.55×10^3	0.85	Enhanced corrosion resistance vs Pt/C; slightly lower ORR activity[23]
NPMC/CNT	2.46×10^3	0.82	Fe-N_4 sites on CNT; ORR mass activity 5–19 $A.g^{-1}$ at 0.8 V [36], [37], [38], high phosphate tolerance [32]
Fe-N-C	1.95×10^3	0.65	ORR mass activity 5–10 $A.g^{-1}$ at 0.8 V vs ~17 $A.g^{-1}$ for Pt/C [30], [32], [33], [34], [35], [36], [37], [38], [39], lower active site density

Transfer coefficients ($\alpha_a = \alpha_c = 1$) and Tafel slopes are identical for all four catalysts. $j_{0,a,ref} = 1.0 \times 10^9$ $A.m^{-3}$ for all catalysts (anode HOR kinetics unchanged).

The polarization curve of all the electrocatalysts follows a similar trend in the low and intermediate current density regimes. At current densities above 1.2 $A.cm^{-2}$, noticeable differences begin to appear. In the high current density region, the cell voltage of Pt/C catalyst is always the highest, and the Fe-N-C catalyst has the lowest polarization performance among the four materials. The deviation

at high current densities points to the coupled effect of ORR kinetics and mass transport on the overall cell performance. The performance ranking Pt/C > Pt-Ir/C > NPMC/CNT > Fe-N-C can be explained by the electrochemical kinetics parameters and the physicochemical properties of each catalyst. Pt/C delivers the highest peak power density (0.453 $W.cm^{-2}$) owing to its combination of the highest $j_{o,c,ref,}$ a well-developed three-phase boundary within the carbon-supported nanoparticle structure, and favorable mass transport characteristics. However, Pt/C does experience phosphate chemisorption on active sites under the H_3PO_4 environment at 180 °C, which partially reduces its effective ORR activity and narrows the performance gap with NPMC/CNT relative to what would be expected from ambient-condition benchmarks alone. Pt-Ir/C achieves a closely comparable power density (0.441 $W.cm^{-2}$) because iridium enhances corrosion resistance and structural stability of the catalyst layer at high temperature, partially compensating for its slightly lower intrinsic ORR activity. The NPMC/CNT possesses a competitive power density of 0.370 $W.cm^{-2}$ due to the high electrical conductivity of the CNT support (~104 $S.m^{-1}$), the large accessible surface area (1000 $m^2.g^{-1}$) and the presence of Fe-N_4 active sites, which have a higher resistance to phosphate poisoning than Pt, making it particularly suited to H_3PO_4-doped PBI environments [32]. Fe-N-C has the lowest power density (0.310 $W.cm^{-2}$), consistent with its lower volumetric activity ($j_{0,c,ref}$ = 0.65× Pt/C) and lower active site density than NPMC/CNT. The difference in performance between the non-precious catalysts and Pt/C is ~15–32%, which is in agreement with reported literature values for Fe-N-C and NPMC/CNT materials under HT-PEMFC conditions [30], [32], [33], [34], [35], [36], [37], [38], [39]. These results confirm that while NPMCs remain below Pt/C in peak power density under present conditions, their greater phosphate poisoning resistance and lower material cost make them technically viable candidates for cost-sensitive HT-PEMFC applications. Table 8 presents a direct comparison of the peak power densities obtained in this study against representative literature values for each catalyst material under HT-PEMFC operating conditions, confirming the physical consistency of the present model with the broader experimental literature.

Table 9: Comparison of peak power densities from this study with representative literature values for each catalyst material under HT-PEMFC operating conditions.

Catalyst	This study (W cm^{-2})	Literature range (W cm^{-2})	Key references
Pt/C	0.453	0.40–0.65	[51, 14]

Pt–Ir/C	0.441	0.38–0.55	[23]
NPMC/CNT	0.370	0.30–0.50	[37, 38]
Fe-N-C	0.310	0.25–0.50	[30, 36, 39]

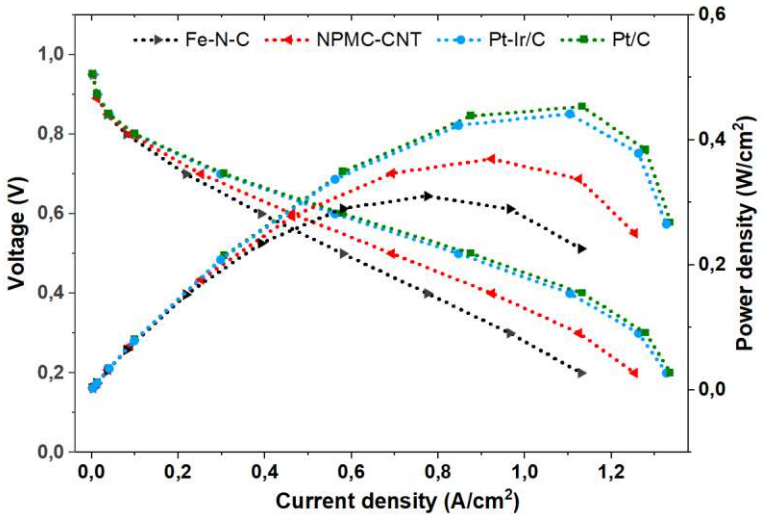


Fig. 14: Polarization curves of different catalyst materials; Fe-N-C, NPMC/CNT, Pt-Ir/C, and Pt/C.

To further characterize the spatial performance distribution in the multi-channel configuration, local current density contour maps were extracted for all 11 channels at each operating voltage and inlet velocity condition, as shown in Fig. 15. At 0.9 V (row a), the current density is low for all channels, regardless of the inlet velocity, consistent with the near-equilibrium electrochemical conditions at near-OCV. At a reduced operating voltage of 0.6 V (row b), a progressive spatial gradient is established: channels closest to the inlet manifold show significantly higher local current density than downstream channels, due to higher local reactant concentration available at the manifold end. This non-uniformity is significantly enhanced at 0.4 V (row c), where the depletion of reactants along the channel length leads to strong concentration gradients that enhance the inter-channel current density variation. The effect of inlet velocity is equally pronounced: at low velocity (V1), the slower reactant supply permits more complete consumption per unit channel length, concentrating the electrochemical activity near the inlet and deepening the downstream gradient.

At high velocity (V3), the greater reactant supply rate partially homogenizes the distribution across channels, although significant non-uniformity persists at 0.4 V, where the local current density exceeds 2 A.cm^{-2} in the channels nearest the inlet manifold (Channel 1) and falls below 0.5 A.cm^{-2} in the most distal channels (Channel 11), representing more than a four-fold inter-channel variation under the highest current density condition examined. These results have direct implications for long-term HT-PEMFC durability. Under a non-isothermal operating environment, regions of elevated current density would be expected to experience higher localized Joule heating, potentially accelerating phosphoric acid redistribution within the GDL and catalyst layer. Although the present isothermal model does not compute the temperature field directly, the spatial current density non-uniformity identified here provides a quantitative basis for locating regions of greatest thermal risk [9, 10], motivating future non-isothermal CFD modelling to quantify these effects. Downstream channels operating under reactant-starved conditions also risk local carbon corrosion at the cathode catalyst layer, a degradation mode well-documented in parallel-channel PEM fuel cell designs. These findings highlight the importance of flow-field optimization, particularly manifold geometry and channel tapering, to minimize inter-channel non-uniformity in scaled multi-channel single-cell HT-PEMFC designs. optimization, particularly manifold geometry, and channel tapering, to minimize inter-channel non-uniformity in scaled multi-channel single-cell HT-PEMFC designs.

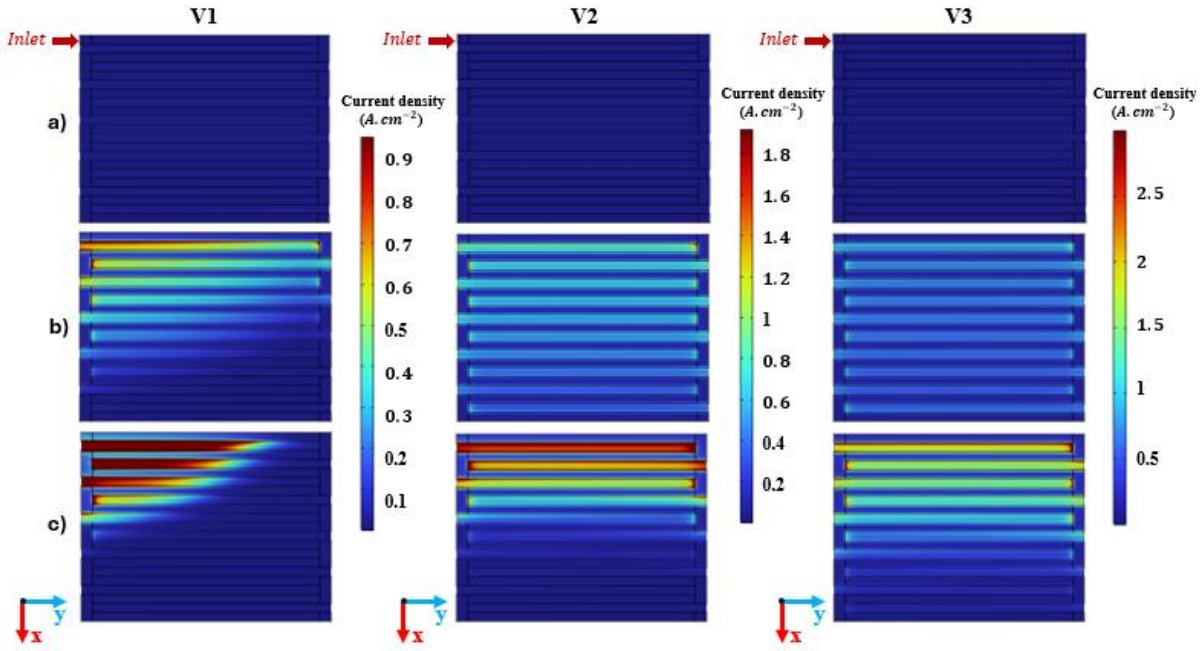


Fig. 15: Current density distribution across the cathode catalyst layer of the 11-channel HT-PEMFC at three operating voltages: (a) 0.9 V, (b) 0.6 V, and (c) 0.4 V, under three inlet velocity

conditions: V1 (low velocity, anode: 0.10 $m.s^{-1}$), V2 (intermediate velocity, anode: 0.5 $m.s^{-1}$), and V3 (high velocity, anode: 1.0 $m.s^{-1}$). The color scale represents the current density in $A.cm^{-2}$.

3.6. Sensitivity Analysis and Benchmark Comparisons

Sensitivity analyses on GDL porosity ($\varepsilon = 0.4 – 0.6$) and permeability ($\kappa = 10^{-11}–10^{-12}\ m^2$) [54] have been performed. According to the Bruggeman correction, the effective enhancement of diffusivity is about 15 % for a 20% increase in porosity. This leads to a 10 % decrease in concentration losses at high current densities [55]. The variation in permeability may lead to pressure drops as high as 25 % [56], illustrating the flow-resistance trade-offs in GDL design. In comparison to established benchmarks, the NPMC electrocatalysts simulated here demonstrate power densities ranging from 0.31 to 0.37 W cm^{-2}. These are competitive with recent findings on Fe-N-C materials reporting power densities up to 0.5 W cm^{-2}, though lower than optimized Pt/C benchmarks of 0.8 W cm^{-2}. Further doping strategies could improve NPMC power density, as described elsewhere [57]. A comparison between the single-channel and multi-channel single-cell configurations reveals that non-uniformities in the multi-channel design produce a 10 – 20% variation in current density across channels, attributable to the flow distribution among parallel channels, and approximately 50% higher pressure losses relative to the single-channel case, emphasizing the need for flow field optimization in scaled single-cell designs. While this study provides insight into HT-PEMFC performance under a range of operating conditions, several limitations arise from the simplifying assumptions adopted. The steady-state isothermal formulation is unable to account for the transient load variations typical of practical operation nor the large temperature gradients that impact reaction kinetics, membrane conductivity, and material degradation. The model also does not incorporate degradation mechanisms such as Ostwald ripening, carbon support corrosion, and phosphoric acid redistribution. Finally, the single-phase (vapour-only) flow assumption precludes analysis of any condensate effects. Future work addressing these aspects will provide a more comprehensive framework for optimizing HT-PEMFC designs.

4. **Conclusion**

The following principal findings were obtained from this three-dimensional CFD investigation of mass transport, pressure drop, and catalyst performance in HT-PEMFCs with H_3PO_4-doped PBI membranes:

1. Flow-field configuration and pressure drop: The single-channel design exhibits significantly lower pressure losses than the multi-channel single-cell configuration (0.8 Pa vs. ~50 Pa anode inlet at 0.9 V), reflecting the higher hydraulic resistance of parallel-channel flow distribution (approximately 12.5× higher). Counterintuitively, inlet pressure drop is consistently higher at 0.9 V than at 0.4 V across both configurations. This isa behavior specific to the vapour-only operating environment of HT-PEMFCs. At near-OCV conditions, minimal reactant consumption preserves gas mass flow rate and dynamic pressure along the channel; at 0.4 V, extensive electrochemical consumption reduces local flow velocity and hence pressure drop. This mechanism is absent in LT-PEMFCs, where liquid water dominates channel hydraulics, and underscores the need to account for HT-PEMFC-specific transport physics in flow-field design.

2. Inlet velocity and reactant distribution. Higher inlet velocities markedly enhanced hydrogen mass transport and utilization, producing a pronounced mole-fraction gradient along the channel, while oxygen consumption remained comparatively stable across all conditions. In the multi-channel configuration, reducing operating voltage combined with increasing inlet velocity improved reactant penetration to downstream channels, yielding more uniform current density distribution and reduced concentration losses.

3. Inter-channel current density non-uniformity. Three-dimensional current density contour maps across all 11 channels reveal significant spatial non-uniformity, particularly at high current density and elevated inlet velocity. Channels nearest the inlet manifold exhibit markedly higher local current density, creating conditions favorable for localized phosphoric acid redistribution and hotspot formation. This non-uniformity underscores the importance of flow-field optimization for long-term PBI membrane durability in multi-channel single-cell HT-PEMFC designs.

4. Catalyst performance. Pt/C and Pt–Ir/C delivered the highest peak power densities (0.453 and 0.441 W cm^{-2}), consistent with their higher cathode reference exchange current densities ($j_{o,c,ref}$ = 3.0×10^3 and 2.55×10^3 $A.m^{-3}$, respectively). NPMC/CNT and Fe-N-C achieved competitive values of 0.370 and 0.310 W cm^{-2}, rationalized through Butler–Volmer scaling ($j_{o,c,ref} = 2.46 \times 10^3$ and 1.95×10^3 $A.m^{-3}$) and their superior resistance to phosphate poisoning in the H_3PO_4-PBI environment. The performance gap between NPMCs and Pt/C is 15–32%, consistent with reported literature values for these catalyst classes under HT-PEMFC conditions. While over 200 CFD studies address HT-PEMFC flow fields, fewer than ten incorporate NPMCs, and none combine multi-channel single-cell pressure-drop analysis with spatially resolved current density maps and literature-grounded NPMC kinetic input values as presented here [13, 48].

Future work. This framework will be extended to incorporate non-isothermal effects, phosphoric acid leaching dynamics, and catalyst-layer microstructure. In parallel, high-entropy non-precious perovskite-based electrocatalysts will be synthesized and experimentally characterized to directly validate and refine the computational models, establishing a quantitative link between catalyst intrinsic activity and cell-scale transport limitation.

Acknowledgements

The authors would like to sincerely thank OCP group for their financial support of the 'Energy, Science Technology / NRG' program, under Specific Agreement Number 175 and OCP foundation for UM6P management start grant 104EQPR19-1 for conducting this manuscript work.

Credit Author Statement

Abdelaziz Samris*: Conceptualization, and complete CFD simulation of HT-PEM fuel cell, Writing – Original Draft Preparation, Corresponding Author. **Khaoula Sarout**: NPMC catalysts review and writing – Original Draft Preparation. **Abdessamad Faik**: Review and editing, Project Administration. **Debajeet K Bora***: Writing – Review and Editing, Supervision, Corresponding Author.

Declaration of Competing Interest: The authors declare the following financial interests/ personal relationships that may be considered as potential competing interests: University Mohammed VI Polytechnic provided Debajeet KUMAR BORA with financial support and administrative support. DEBAJEET KUMAR BORA reports a relationship with University Mohammed VI Polytechnic that includes employment. The author declares no conflict of interest. If there are other authors, they declare that they have no known competing financial interests or personal relationships that could have appeared to influence the work reported in this article.

Data availability: Data is available on request.

List of Symbols

ϵ_{P} : Volume fraction of CL porosity

ρ : Density of the gas mixtures (kg.cm^{-3})

μ : dynamic viscosity of the gas mixture ($kg.m^{-1}.s^{-1}$)

ω : mass fraction

x : molar fraction

D_{ij} : binary diffusion coefficient

F : Faraday constant

R : Ideal-gas constant ($8.314\ J.mol^{-1}.K^{-1}$)

T : Temperature (K)

$C_{O_2}^{ref}$: Reference concentration of oxygen ($mol.m^{-3}$)

$C_{H_2}^{ref}$: Reference concentration of hydrogen ($mol.m^{-3}$)

$j_{0,a}^{ref}$: Anode reference exchange current densities ($A.m^{-3}$)

$j_{0,c}^{ref}$: Cathode reference exchange current densities ($A.m^{-3}$)

η : Over potential (V)

E_c : Activation energy in oxygen reduction reaction ($J.mol^{-1}$)

Abbreviations

a : Anode.

c : Cathode.

m : Membrane.

s : Solid.

l : liquid.

pt : Platinum.

HOR : Hydrogen oxidation reaction.

ORR : Oxygen reduction reaction.

GDL : Gas diffusion layer.

MPL : Microporous layer.

CL : Catalyst layer.

PEM : Proton exchange membrane.

CNFs: carbon nanofibers

CNTs: Nanocarbon materials such as carbon nanotubes

ECSA: electrochemically active surface area

M–N–C : metal–nitrogen–carbon

PA: phosphoric acid

PBI: Polybenzimidazole

PGM: platinum-group metal

References

[1] P. R. Chowdhury and A. C. Gladen, “Design of Flow Fields for High-Temperature PEM Fuel Cells Using Computational Fluid Dynamics,” *Energies (Basel).*, vol. 17, no. 19, p. 4898, Oct. 2024, doi: 10.3390/EN17194898/S1.

[2] Q. Deng *et al.*, “Mass transfer evaluation of full-scale PEMFC and flow field optimization based on the brachistochrone principle,” *Appl. Energy*, vol. 402, Dec. 2025, doi: 10.1016/j.apenergy.2025.126928.

[3] S. Bhogilla, A. Pandoh, and U. R. Singh, “Cogeneration system combining reversible PEM fuel cell, and metal hydride hydrogen storage enabling renewable energy storage: Thermodynamic performance assessment,” *Int. J. Hydrogen Energy*, vol. 52, pp. 1147–1155, Jan. 2024, doi: 10.1016/J.IJHYDENE.2023.08.028.

[4] X. Yang *et al.*, “Durable Proton Exchange Membrane Based on Polymers of Intrinsic Microporosity for Fuel Cells,” *Advanced Materials*, vol. 37, no. 19, p. 2419534, May 2025, doi: 10.1002/ADMA.202419534;ISSUE:ISSUE:DOI.

[5] N. A. A. Qasem and G. A. Q. Abdulrahman, “A Recent Comprehensive Review of Fuel Cells: History, Types, and Applications,” *Int. J. Energy Res.*, vol. 2024, no. 1, p. 7271748, Jan. 2024, doi: 10.1155/2024/7271748.

[6] M. Baudy *et al.*, “Validation of a post-processing methodology to readjust the voltage of a high-temperature PEM fuel cell according to the atmospheric pressure on a 2753h aging test at different constant currents,” *Int. J. Hydrogen Energy*, vol. 97, pp. 727–737, Jan. 2025, doi: 10.1016/J.IJHYDENE.2024.11.322.

[7] N. Bevilacqua, M. G. George, S. Galbiati, A. Bazylak, and R. Zeis, “Phosphoric Acid Invasion in High Temperature PEM Fuel Cell Gas Diffusion Layers,” *Electrochim. Acta*, vol. 257, pp. 89–98, Dec. 2017, doi: 10.1016/J.ELECTACTA.2017.10.054.

[8] M. Zhou, A. Ali, J. Zhu, S. S. Araya, and V. Liso, “Evaluation of thermal cycling on durability and PA loss in high temperature PEM fuel cells,” *J. Power Sources*, vol. 623, p. 235411, Dec. 2024, doi: 10.1016/J.JPOWSOUR.2024.235411.

[9] N. Narayanan, B. Ravichandran, I. Emayavaramban, H. Liu, and H. Su, “Advancements in Non-Precious Metal Catalysts for High-Temperature Proton-

Exchange Membrane Fuel Cells: A Comprehensive Review," *Catalysts 2025, Vol. 15, Page 775*, vol. 15, no. 8, p. 775, Aug. 2025, doi: 10.3390/CATAL15080775.

[10] U. Raj Aryal, B. Hasa, and G. Zhu, "Three-dimensional simulation of high temperature ion-pair PEM fuel cell integrated with agglomerate sub-model of cathode catalyst layer," *Energy Convers. Manag.*, vol. 324, p. 119289, Jan. 2025, doi: 10.1016/J.ENCONMAN.2024.119289.

[11] S. K. Das and H. A. Gibson, "Three-dimensional multi-physics modeling and simulation for assessment of mass transport impact on the performance of a high temperature polymer electrolyte membrane fuel cell," *J. Power Sources*, vol. 499, p. 229844, Jul. 2021, doi: 10.1016/J.JPOWSOUR.2021.229844.

[12] A. Samris and H. Mounir, "Using a three-dimensional computational fluid dynamics model and an agglomerate model to investigate the effect of varying agglomerate parameters and output voltages on proton exchange membrane fuel cell performance," *Heliyon*, vol. 10, no. 11, p. e32277, Jun. 2024, doi: 10.1016/J.HELIYON.2024.E32277.

[13] A. Samris and H. Mounir, "Three-dimensional computational fluid dynamics (3D-CFD) simulation of hydrogen transport to investigate the effect of output voltage and inlet anode velocity on proton exchange membrane fuel cell performances," *Results Chem.*, vol. 13, p. 101929, Jan. 2025, doi: 10.1016/J.RECHEM.2024.101929.

[14] V. K. Krastev, M. Baldelli, L. Bartolucci, F. Donato, M. Kheir Rouz, and V. Mulone, "Optimal cathode design of a single high temperature PEM fuel cell: A computational study," *Int. J. Hydrogen Energy*, vol. 142, pp. 80–89, Jun. 2025, doi: 10.1016/J.IJHYDENE.2025.05.346.

[15] V. K. Krastev, G. Falcucci, E. Jannelli, M. Minutillo, and R. Cozzolino, "3D CFD modeling and experimental characterization of HT PEM fuel cells at different anode gas compositions," *Int. J. Hydrogen Energy*, vol. 39, no. 36, pp. 21663–21672, Dec. 2014, doi: 10.1016/J.IJHYDENE.2014.09.015.

[16] A. Samir, M. S. Maowwad, M. A. Farahat, and M. Talaat, "Numerical investigation of high-temperature proton exchange membrane fuel cell conductivity at different parameters," *Scientific Reports 2025 15:1*, vol. 15, no. 1, pp. 5318-, Feb. 2025, doi: 10.1038/s41598-025-89277-6.

[17] N. Seselj, S. M. Alfaro, E. Bompolaki, L. N. Cleemann, T. Torres, and K. Azizi, "Catalyst Development for High-Temperature Polymer Electrolyte Membrane Fuel Cell (HT-PEMFC) Applications," *Advanced Materials*, vol. 35, no. 40, p. 2302207, Oct. 2023, doi: 10.1002/ADMA.202302207;PAGE:STRING:ARTICLE/CHAPTER.

[18] H. Ma, Y. Tong, Y. M. Hung, and X. Wang, “Progress on the durability of catalyst layer interfaces in proton-exchange membrane fuel cells,” *Process Safety and Environmental Protection*, vol. 192, pp. 358–377, Dec. 2024, doi: 10.1016/J.PSEP.2024.10.047.

[19] I. Laghryb, M. Malki, N. Yousfi Steiner, C. D. Barrett, and H. El Kadiri, “Catalyst degradation in proton exchange membrane fuel cells: Mechanisms, investigation techniques, and predictive modelling,” *Int. J. Hydrogen Energy*, vol. 145, pp. 496–507, Jul. 2025, doi: 10.1016/J.IJHYDENE.2025.06.052.

[20] M. Yusro and V. Hacker, “Advantages of ordered catalyst layers in PEMFCs: theoretical perspectives and future development,” *Sustain. Energy Fuels*, vol. 9, no. 10, pp. 2625–2650, May 2025, doi: 10.1039/D5SE00028A.

[21] S. Akula *et al.*, “Mesoporous textured Fe-N-C electrocatalysts as highly efficient cathodes for proton exchange membrane fuel cells,” *J. Power Sources*, vol. 520, p. 230819, Feb. 2022, doi: 10.1016/J.JPOWSOUR.2021.230819.

[22] P. Lauf *et al.*, “Benchmarking Performance and Degradation of Pt Supported on Different Carbons for PEMFC Applications Using Gas Diffusion Electrode Half-Cell,” *ACS Appl. Energy Mater.*, vol. 8, no. 12, pp. 7939–7947, Jun. 2025, doi: 10.1021/ACSAEM.5C00184.

[23] Y. Wang *et al.*, “Ir-Pt/C composite with high metal loading as a high-performance anti-reversal anode catalyst for proton exchange membrane fuel cells,” *Int. J. Hydrogen Energy*, vol. 47, no. 26, pp. 13101–13111, Mar. 2022, doi: 10.1016/J.IJHYDENE.2022.02.065.

[24] P. Lauf *et al.*, “Benchmarking Performance and Degradation of Pt Supported on Different Carbons for PEMFC Applications Using Gas Diffusion Electrode Half-Cell,” *ACS Appl. Energy Mater.*, vol. 8, no. 12, pp. 7939–7947, Jun. 2025, doi: 10.1021/ACSAEM.5C00184.

[25] S. Tzelepis, K. A. Kavadias, and G. E. Marnellos, “A Three-Dimensional Simulation Model for Proton Exchange Membrane Fuel Cells with Conventional and Bimetallic Catalyst Layers,” *Energies 2023, Vol. 16, Page 4086*, vol. 16, no. 10, p. 4086, May 2023, doi: 10.3390/EN16104086.

[26] J. G. Buschermöhle *et al.*, “Fe–Sn–N–C Catalysts: Advancing Oxygen Reduction Reaction Performance,” *ACS Catal.*, vol. 15, no. 6, pp. 4477–4488, Mar. 2025, doi: 10.1021/ACSCATAL.4C06338.

[27] “Nanostructured Nonprecious Metal Catalysts for Oxygen Reduction Reaction - Recherche Google.” Accessed: Jun. 22, 2026. [Online]. Available: https://www.google.com/search?q=Nanostructured+Nonprecious+Metal+Catalysts+

for+Oxygen+Reduction+Reactionrlz=1C1FHFK_frMA1157MA1157oq=Nanostructured+Nonprecious+Metal+Catalysts+for+Oxygen+Reduction+Reactiongs_lcrp=EgZjaHJvbWUyBggAEEUYOdIBBzkyNWowajeoAgCwAgAsourceid=chromeie=UTF-8

[28] A. Meftahi *et al.*, "Carbon nanotubes and nanofibers as building blocks for the future: Structure, synthesis, properties, and functionalization perspectives," *Materials Science and Engineering: B*, vol. 322, p. 118622, Dec. 2025, doi: 10.1016/J.MSEB.2025.118622.

[29] Y. Cai *et al.*, "Impedance Spectroscopy Characterization of PEM Fuel Cells with Fe-N-C-Based Cathodes," *J. Electrochem. Soc.*, vol. 166, no. 10, p. F653, Jun. 2019, doi: 10.1149/2.1431910JES.

[30] D. Xue and J.-N. Zhang, "Recent progress of antipoisoning catalytic materials for high temperature proton exchange membrane fuel cells doped with phosphoric acid," *Industrial Chemistry Materials*, vol. 2, no. 2, pp. 173–190, May 2024, doi: 10.1039/D3IM00101F.

[31] L. Gong, L. Tao, L. Wang, X. Z. Fu, and S. Wang, "Focus on the catalysts to resist the phosphate poisoning in high-temperature proton exchange membrane fuel cells," *Chinese Journal of Catalysis*, vol. 68, pp. 155–176, Jan. 2025, doi: 10.1016/S1872-2067(24)60162-2.

[32] Y. Hu, J. O. Jensen, C. Pan, L. N. Cleemann, I. Shypunov, and Q. Li, "Immunity of the Fe-N-C catalysts to electrolyte adsorption: Phosphate but not perchloric anions," *Appl. Catal. B*, vol. 234, pp. 357–364, Oct. 2018, doi: 10.1016/J.APCATB.2018.03.056.

[33] S. Li, L. Shi, Y. Guo, J. Wang, D. Liu, and S. Zhao, "Selective oxygen reduction reaction: mechanism understanding, catalyst design and practical application," *Chem. Sci.*, vol. 15, no. 29, pp. 11188–11228, Jul. 2024, doi: 10.1039/D4SC02853H.

[34] A. M. Gómez-Marín and J. M. Feliu, "Oxygen reduction on platinum single crystal electrodes," *Encyclopedia of Interfacial Chemistry: Surface Science and Electrochemistry*, pp. 820–830, Jan. 2018, doi: 10.1016/B978-0-12-409547-2.13333-5.

[35] H. Ren *et al.*, "Fe/N/C Nanotubes with Atomic Fe Sites: A Highly Active Cathode Catalyst for Alkaline Polymer Electrolyte Fuel Cells," *ACS Catal.*, vol. 7, no. 10, pp. 6485–6492, Oct. 2017, doi: 10.1021/ACSCATAL.7B02340.

[36] R. Li, Y. Hao, Y. Liu, P. Li, and J. Liu, "Short nanotubular Fe-N-C catalysts with curved catalytic sites and contributing regions for oxygen reduction reaction," *J.*

Alloys Compd., vol. 984, p. 174002, May 2024, doi: 10.1016/J.JALLCOM.2024.174002.

[37] M. Rauf *et al.*, "Novel Heteroatom-Doped Fe/N/C Electrocatalysts with Superior Activities for Oxygen Reduction Reaction in Both Acid and Alkaline Solutions," *Front. Chem.*, vol. 8, p. 521549, Feb. 2020, doi: 10.3389/FCHEM.2020.00078/TEXT.

[38] M. Liu, J. Liu, Z. Li, Y. Song, and F. Wang, "A silica-confined strategy for completely atomic level Fe(II)-N-C catalysts with a non-planar structure toward oxygen reduction reaction," *J. Catal.*, vol. 370, pp. 21–29, Feb. 2019, doi: 10.1016/J.JCAT.2018.11.039.

[39] D. Banham *et al.*, "Critical advancements in achieving high power and stable nonprecious metal catalyst–based MEAs for real-world proton exchange membrane fuel cell applications," *Sci. Adv.*, vol. 4, no. 3, p. eaar7180, Mar. 2018, doi: 10.1126/SCIADV.AAR7180.

[40] Y. J. Sa *et al.*, "A General Approach to Preferential Formation of Active Fe–Nx Sites in Fe–N/C Electrocatalysts for Efficient Oxygen Reduction Reaction," *J. Am. Chem. Soc.*, vol. 138, no. 45, pp. 15046–15056, Nov. 2016, doi: 10.1021/JACS.6B09470.

[41] B. Li and R. Jervis, "Advancing Fe–N–C catalysts: synthesis strategies and performance enhancements for fuel cell applications," *Energy Advances*, vol. 4, no. 12, pp. 1412–1425, Oct. 2025, doi: 10.1039/D5YA00256G.

[42] M. A. Z. G. Sial, Z. M. Bhat, and M. Qamar, "Stability Stressors in Electrocatalysis: Mechanistic Origins and Mitigation Strategies for Durable ORR Catalysts," *Adv. Sustain. Syst.*, vol. 10, no. 5, p. e70511, May 2026, doi: 10.1002/ADSU.70511.

[43] F. Daneshvar, H. Chen, K. Noh, and H. J. Sue, "Critical challenges and advances in the carbon nanotube–metal interface for next-generation electronics," *Nanoscale Adv.*, vol. 3, no. 4, p. 942, Feb. 2021, doi: 10.1039/D0NA00822B.

[44] Y. Chen, L. Meng, H. Sun, H. Lin, and S. Sun, "Emerging strategies for durable Pt catalysts in PEMFCs," *Chem. Sci.*, vol. 17, no. 6, pp. 2897–2912, Feb. 2026, doi: 10.1039/D5SC08221H.

[45] N. Narayanan, B. Ravichandran, I. Emayavaramban, H. Liu, and H. Su, "Advancements in Non-Precious Metal Catalysts for High-Temperature Proton-Exchange Membrane Fuel Cells: A Comprehensive Review," *Catalysts 2025, Vol. 15, Page 775*, vol. 15, no. 8, p. 775, Aug. 2025, doi: 10.3390/CATAL15080775.

[46] J. Müller-Hülstede *et al.*, “What determines the stability of Fe-N-C catalysts in HT-PEMFCs?” *Int. J. Hydrogen Energy*, vol. 50, pp. 921–930, Jan. 2024, doi: 10.1016/J.IJHYDENE.2023.09.190.

[47] P. R. Chowdhury and A. C. Gladen, “Design of Flow Fields for High-Temperature PEM Fuel Cells Using Computational Fluid Dynamics,” *Energies (Basel).*, vol. 17, no. 19, p. 4898, Oct. 2024, doi: 10.3390/EN17194898/S1.

[48] C. Neofytidis, F. Paloukis, N. Athanasopoulos, S. G. Neophytides, and M. K. Daletou, “Efficient high temperature PEMFC metallic stack with innovative two-phase liquid cooling,” *Energy Convers. Manag.*, vol. 283, p. 116944, May 2023, doi: 10.1016/J.ENCONMAN.2023.116944.

[49] Y. H. Jeong *et al.*, “Investigation of electrolyte leaching in the performance degradation of phosphoric acid-doped polybenzimidazole membrane-based high temperature fuel cells,” *J. Power Sources*, vol. 363, pp. 365–374, Sep. 2017, doi: 10.1016/J.JPOWSOUR.2017.07.109.

[50] D. G. Caglayan, B. Sezgin, Y. Devrim, and I. Eroglu, “Three-dimensional non-isothermal model development of high temperature PEM Fuel Cells,” *Int. J. Hydrogen Energy*, vol. 43, no. 23, pp. 10834–10841, Jun. 2018, doi: 10.1016/J.IJHYDENE.2018.01.176.

[51] E. U. Ubong, Z. Shi, and X. Wang, “Three-Dimensional Modeling and Experimental Study of a High Temperature PBI-Based PEM Fuel Cell,” *J. Electrochem. Soc.*, vol. 156, no. 10, p. B1276, Aug. 2009, doi: 10.1149/1.3203309.

[52] H. Wu, X. Li, and P. Berg, “On the modeling of water transport in polymer electrolyte membrane fuel cells,” *Electrochim. Acta*, vol. 54, no. 27, pp. 6913–6927, Nov. 2009, doi: 10.1016/J.ELECTACTA.2009.06.070.

[53] M. I. Rosli, B. H. Lim, E. H. Majlan, T. Husaini, W. R. W. Daud, and S. F. Lim, “Performance Analysis of PEMFC with Single-Channel and Multi-Channels on the Impact of the Geometrical Model,” *Energies 2022, Vol. 15, Page 7960*, vol. 15, no. 21, p. 7960, Oct. 2022, doi: 10.3390/EN15217960.

[54] P. Feng, Z. Li, L. Liu, L. Tan, and Y. Zhang, “Improving PEMFC performance with gradient porosity GDL designs: A multiscale simulation study,” *Renew. Energy*, vol. 256, p. 124467, Jan. 2026, doi: 10.1016/J.RENENE.2025.124467.

[55] J. Zhang, D. Xuan, S. Liu, and C. Chen, “Influence and Optimization of Gas Diffusion Layer Porosity Distribution along the Flow Direction on the Performance of Proton Exchange Membrane Fuel Cells,” *ACS Omega*, vol. 9, no. 1, pp. 239–251, Jan. 2023, doi: 10.1021/ACSOMEGA.3C03671.

[56] H. Lei, Y. Xia, and G. Hu, “Effects of Inhomogeneous Gas Diffusion Layer Properties on the Transportation Phenomenon and Performances of Proton-Exchange Membrane Fuel Cells,” *ACS Omega*, vol. 9, no. 8, pp. 9383–9395, Feb. 2024, doi: 10.1021/ACSOMEGA.3C08756.

[57] Q. Meyer, C. Yang, Y. Cheng, and C. Zhao, “Overcoming the Electrode Challenges of High-Temperature Proton Exchange Membrane Fuel Cells,” *Electrochemical Energy Reviews 2023 6:1*, vol. 6, no. 1, pp. 16-, Apr. 2023, doi: 10.1007/S41918-023-00180-Y.